



HAL
open science

ALMA-IMF

M. Armante, A. Gusdorf, F. Louvet, F. Motte, Y. Pouteau, P. Lesaffre, R. Galván-Madrid, P. Dell'ova, M. Bonfand, T. Nony, et al.

► **To cite this version:**

M. Armante, A. Gusdorf, F. Louvet, F. Motte, Y. Pouteau, et al.. ALMA-IMF. Astronomy & Astrophysics - A&A, 2024, 686, pp.A122. 10.1051/0004-6361/202347595 . hal-04601410

HAL Id: hal-04601410

<https://hal.science/hal-04601410v1>

Submitted on 4 Jun 2024

HAL is a multi-disciplinary open access archive for the deposit and dissemination of scientific research documents, whether they are published or not. The documents may come from teaching and research institutions in France or abroad, or from public or private research centers.






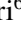




L'archive ouverte pluridisciplinaire **HAL**, est destinée au dépôt et à la diffusion de documents scientifiques de niveau recherche, publiés ou non, émanant des établissements d'enseignement et de recherche français ou étrangers, des laboratoires publics ou privés.



Distributed under a Creative Commons Attribution 4.0 International License

ALMA-IMF

X. The core population in the evolved W33-Main (G012.80) protocluster

M. Armante^{1,2}, A. Gusdorf^{1,2}, F. Louvet³ , F. Motte³, Y. Pouteau³, P. Lesaffre^{1,2}, R. Galván-Madrid⁴ ,
P. Dell’Ova^{1,2}, M. Bonfand⁵ , T. Nony⁴ , N. Brouillet⁶, N. Cunningham³, A. Ginsburg⁷, A. Men’shchikov⁸ ,
S. Bontemps⁶, D. Díaz-González⁴ , T. Csengeri⁶, M. Fernández-López⁹, M. González⁸ , F. Herpin⁶, H.-L. Liu^{10,11},
P. Sanhueza^{12,13} , A.M. Stutz¹⁰ , and M. Valeille-Manet⁶ 

¹ Laboratoire de Physique de l’Ecole Normale Supérieure, ENS, Université PSL, CNRS, Sorbonne Université, Université Paris Cité, 75005 Paris, France

e-mail: melanie.armante@phys.ens.fr

² Observatoire de Paris, Université PSL, Sorbonne Université, LERMA, 75014 Paris, France

³ Univ. Grenoble Alpes, CNRS, IPAG, 38000 Grenoble, France

⁴ Instituto de Radioastronomía y Astrofísica, Universidad Nacional Autónoma de México, Morelia, Michoacán 58089, Mexico

⁵ Depts. of Astronomy & Chemistry, University of Virginia, Charlottesville, VA 22904, USA

⁶ Laboratoire d’astrophysique de Bordeaux, Univ. Bordeaux, CNRS, B18N, allée Geoffroy Saint-Hilaire, 33615 Pessac, France

⁷ Department of Astronomy, University of Florida, PO Box 112055, USA

⁸ Université Paris Cité, Université Paris-Saclay, CEA, CNRS, AIM, 91191, Gif-sur-Yvette, France

⁹ Instituto Argentino de Radioastronomía (CCT-La Plata, CONICET; CICPBA), C.C. No. 5, 1894, Villa Elisa, Buenos Aires, Argentina

¹⁰ Departamento de Astronomía, Universidad de Concepción, Casilla 160-C, Concepción, Chile

¹¹ Department of Astronomy, Yunnan University, Kunming, 650091, PR China

¹² Department of Astronomical Science, SOKENDAI (The Graduate University for Advanced Studies), 2-21-1 Osawa, Mitaka, Tokyo 181-8588, Japan

¹³ Instituto Argentino de Radioastronomía (CCT-La Plata, CONICET; CICPBA), C.C. No. 5, 1894, Villa Elisa, Buenos Aires, Argentina

Received 28 July 2023 / Accepted 19 December 2023

ABSTRACT

Context. One of the central questions in astrophysics is the origin of the initial mass function (IMF). It is intrinsically linked to the processes from which it originates, and hence its connection with the core mass function (CMF) must be elucidated.

Aims. We aim to measure the CMF in the evolved W33-Main star-forming protocluster to compare it with CMF recently obtained in other Galactic star-forming regions, including the ones that are part of the ALMA-IMF program.

Methods. We used observations from the ALMA-IMF large programme: $\sim 2' \times 2'$ maps of emission from the continuum and selected lines at 1.3 mm and 3 mm observed by the ALMA 12 m only antennas. Our angular resolution was typically $1''$, that is, ~ 2400 au at a distance of 2.4 kpc. The lines we analysed are CO (2–1), SiO (5–4), N_2H^+ (1–0), $H41\alpha$ as well as $He41\alpha$ blended with $C41\alpha$. We built a census of dense cores in the region, and we measured the associated CMF based on a core-dependent temperature value.

Results. We confirmed the ‘evolved’ status of W33-Main by identifying three H II regions within the field, and to a lesser extent based on the number and extension of N_2H^+ filaments. We produced a filtered core catalogue of 94 candidates that we refined to take into account the contamination of the continuum by free-free and line emission, obtaining 80 cores with masses that range from 0.03 to $13.2 M_\odot$. We fitted the resulting high-mass end of the CMF with a single power law of the form $N(\log(M)) \propto M^\alpha$, obtaining $\alpha = -1.44^{+0.16}_{-0.22}$, which is slightly steeper but consistent with the Salpeter index. We categorised our cores as prestellar and protostellar, mostly based on outflow activity and hot core nature. We found the prestellar CMF to be steeper than a Salpeter-like distribution, and the protostellar CMF to be slightly top heavy. We found a higher proportion of cores within the H II regions and their surroundings than in the rest of the field. We also found that the cores’ masses were rather low (maximum mass of $\sim 13 M_\odot$).

Conclusions. We find that star formation in W33-Main could be compatible with a ‘clump-fed’ scenario of star formation in an evolved cloud characterised by stellar feedback in the form of H II regions, and under the influence of massive stars outside the field. Our results differ from those found in less evolved young star-forming regions in the ALMA-IMF program. Further investigations are needed to elucidate the evolution of late CMFs towards the IMF over statistically significant samples.

Key words. stars: formation – stars: low-mass – stars: massive – stars: protostars – ISM: clouds – submillimeter: ISM

1. Introduction

In 1955, [Edwin Salpeter \(1955\)](#) inferred that the probability (ξ) of the creation of stars of a given mass at a particular time can be approximated by $\xi \approx 0.03(\frac{M}{M_\odot})^{-1.35}$ for masses between

0.4 and $10.0 M_\odot$, independently of time. For masses larger than $10 M_\odot$, he observed a steep drop of ξ . Considering the small amount of observations at his disposal as well as their resolution, he was unable to make definitive conclusions on the apparent lack of massive stars. For decades after this result was obtained,

the initial mass function (IMF) was observationally studied in the solar neighbourhood (≤ 150 pc), and the model was fine-tuned. Based on these local observations, it appeared that the IMF could be represented by a log-normal function peaking at stellar masses around $0.2\text{--}0.3 M_{\odot}$, connected to a known power-law tail $\frac{dN}{d\log M} \propto M^{\alpha}$ with $\alpha = -1.35$. This power-law dominates for masses larger than $1 M_{\odot}$, which becomes $N(\geq \log(M)) \propto M^{-1.35}$ in its complementary cumulative form (e.g. Bastian et al. 2010; Kroupa et al. 2013). In this article, we hence refer to the -1.35 factor as the ‘Salpeter slope’. Another outcome of these local observations was the apparent universality of the IMF. Its origin was questioned, and the mass distribution of stars’ progenitors was subsequently studied. To this aim, molecular cloud fragments were observed, and cores were defined as the smallest spatially resolved (~ 0.01 pc), gravitationally bound, and dense ($n_{\text{H}_2} = 10^4\text{--}10^8 \text{ cm}^{-3}$) cloud fragments that are expected to form single stars or multiple systems. Thus, the definition of cores was intrinsically linked to the angular resolution of telescopes from the beginning. With this definition, studies of the mass distribution of cores, that is, the core mass function (CMF), were conducted in Gould Belt clouds, and solar neighbourhood star-forming regions that mostly form solar-type stars (e.g. Motte et al. 1998, 2001; Testi & Sargent 1998; Enoch et al. 2008; Könyves et al. 2015, 2020; Takemura et al. 2021). They all reported CMF slopes with a high-mass end similar to the Salpeter one. This led to the conclusion that the IMF inherits its shape from the CMF (Motte et al. 1998; André et al. 2014). Under this assumption, the final mass of the star is entirely set by the mass reservoir of the core. In this scenario, stepping from the CMF to the IMF would only consist in a shift to lower masses, described by a conversion efficiency of core mass into star mass, which is also called star formation efficiency (ϵ_{core}). Additionally, this scenario was based on a ‘core-collapse’ or quasi-static star formation scenario, where the available mass to form a star originates from its core.

Most of these findings were made possible by observing star-forming regions in the far-infrared to millimetre wavelength regimes at core scales. In the last decade, significant progresses have been made in interferometry with the commissioning of the ALMA (Atacama Large Millimeter/sub-millimetre Array) in the sub-millimetre and millimetre wavelength range. This telescope opened the possibility to observe more distant (≥ 1 kpc), high-mass star-forming regions with spatial resolution down to core scales (~ 0.01 pc). In other words, its angular resolution made it possible to sample the high-mass end of the CMF. One of the first ALMA observations of a distant star-forming region of the Galaxy (at ~ 5.5 kpc, Zhang et al. 2014) was dedicated to W43-MM1, a massive filament in the W43 high-mass star-forming region. The entire W43 complex had previously been observed and characterised down to $5''$ angular resolution (Nguyen Luong et al. 2011, 2013; Carlhoff et al. 2013; Louvet et al. 2014, 2016). At this $5''$ resolution of NOEMA available at the time, a dozen of prestellar and protostellar cores were identified over the few parsecs of the whole W43-MM1 filament. At the $1''$ resolution of ALMA, Motte et al. (2018b) were able to identify more than a hundred cores in a sub-field of W43-MM1. With this core sample, they built a CMF with a high-mass tail significantly flatter than the Salpeter IMF (with a power-law index of $\alpha = -0.96 \pm 0.12$). Following this study, similar ‘top-heavy’ CMFs were measured based on ALMA observations in distant (≥ 1 kpc) high-mass star-forming clusters (Sanhueza et al. 2019 and Kong 2019). Interestingly, observational studies had begun to exhibit a similar trend in the IMF itself, in

a variety of environments. Recent observations of young massive clusters in the Milky Way (Lu et al. 2013; Maia et al. 2016; Hosek et al. 2019), in nearby galaxies (Schneider et al. 2018), and in high-redshift galaxies (Smith 2014; Zhang et al. 2018) measured a larger proportion of high-mass stars than predicted by the Salpeter IMF, resulting in top-heavy IMFs. These results put into question the link between the CMF and the IMF, as well as the universality of the IMF.

In order to measure the CMF in a diversity of star-forming regions, the ALMA-IMF¹ Large Programme was proposed. The complete description of the programme can be found in Paper I by Motte et al. (2022), hereafter M22. ALMA-IMF provides an unprecedented database corresponding to continuum images (see Paper II, Ginsburg et al. 2022, hereafter G22, for details) and line cubes (see Paper VII, Cunningham et al. 2023, hereafter C23, for details), which are homogeneously reduced and qualified in detail. A sample of 15 massive ($2\text{--}33 \times 10^3 M_{\odot}$) nearby ($2.5\text{--}5.5$ kpc) protoclusters were observed. Each individual protocluster was imaged with the ALMA interferometer with ~ 2000 au spatial resolution. These 15 regions were chosen to cover the widest possible range in density and evolutionary stage of embedded protoclusters: young (six regions), intermediate (five), and evolved (four). This classification was initially based on the flux detected towards these regions at mid-infrared wavelengths (Csengeri et al. 2017). It was then refined based on the bolometric luminosity-to-mass ratios, and definitely established based on ALMA-IMF observations (1.3 mm to 3 mm flux ratio and estimated free-free emission flux density, and associated with faint, ultra-compact, strong or regular H II regions; see M22). A first, global, study of the core population of all 15 ALMA-IMF protoclusters is in progress (Louvet et al. 2023).

In W43-MM2, and MM3, Pouteau et al. (2022) found 205 cores with mass ranging from $\sim 0.1 M_{\odot}$ to $70 M_{\odot}$ (Paper III). The resulting CMF has a power-law index for the high-mass tail of $\alpha = -0.95 \pm 0.04$. Pouteau et al. (2023) subsequently divided W43-MM2, and MM3 into six sub-regions (Paper VI). They studied how their CMF power-law slope index varies with cloud characteristics (such as the PDF of the gas column density). They proposed that star formation bursts result in the flattening of the CMF high-mass tail throughout the initial phases of cloud and star formation. In the young W43-MM1, MM2, and MM3 regions, Nony et al. (2023) also studied the evolution of the CMF with core evolution (Paper V). They found that the CMF’s slope is either Salpeter or top-heavy in prestellar and protostellar stages, respectively. In order to better understand the evolution of the CMF with the evolutionary stage of a protocluster, evolved regions must also be studied in detail. We present an in-depth study of one of the four evolved ALMA-IMF protoclusters, W33-Main, also known as G012.80. The motivation for our additional work with respect to that of Louvet et al. (2023) is that we explicitly investigated and quantified the influence of H II regions on the CMF, and we attempted to build differentiated CMFs for prestellar and protostellar sub-populations in our core sample.

In this paper, we first present the features of the region that support its classification as an evolved, massive, star-forming site in Sect. 2. We then present the continuum and line data obtained in the frame of the ALMA-IMF programme in the W33-Main region in Sect. 3. We produce catalogues of continuum sources that are likely to be cores in Sect. 4. We also estimate their evolutionary stage, based on infrared continuum and millimetre line emission to distinguish between prestellar and protostellar

¹ <https://almainf.com/>

sources in Sect. 5. In Sect. 6, we measure the mass of the cores and present the resulting CMF. With aims to study the time evolution of the CMF, we produce and discuss the CMF we obtained for the prestellar and protostellar core populations, respectively, and discuss the impacts of the H II regions on the core mass distribution in Sect. 7. We summarise and conclude in Sect. 8.

2. The G012.80 region

The W33 complex was first detected as a thermal radio source in the 1.4 GHz survey of Westerhout (1958). A parallax study of this complex by Immer et al. (2013) located the W33 complex in the Scutum spiral arm, in the first quadrant of the Galaxy, at a distance of $2.40_{-0.15}^{+0.17}$ kpc. The target of our study is the W33-Main substructure, a star-forming region that was associated with the 33–38 km s⁻¹ velocity range. At this distance, an angular beam size of 15' corresponds to a physical scale of about 10 pc, and the OB star cluster associated with W33-Main has spectral types ranging from O7.5 to B1.5. Using ATLASGAL (APEX Telescope Large Area Survey of the Galaxy; Schuller et al. 2009) data, combined with observations from the APEX (Atacama Pathfinder EXperiment) telescope at 280 GHz, SMA (Submillimetre Array; with short-spacings from the IRAM 30 m telescope) at 230 GHz, and various existing datasets, Immer et al. (2014; hereafter I14) built the most comprehensive view of the W33 region to date. W33-Main is the most massive ($(4.0 \pm 2.5) \times 10^3 M_{\odot}$) and luminous ($4.49 \times 10^5 L_{\odot}$) sub-region they identified. In an aperture of 100'', they measured a cold dust temperature of 42.5 ± 12.6 K with a spectral emissivity index of $\beta = 1.2$, and a gas temperature comprised between 40 and 100 K. Based on its chemical composition and the presence of radio emission, they classified it as an H II region, similar to the 'evolved' status of ALMA-IMF fields.

Shortly after, Messineo et al. (2015) investigated W33's star formation based on near-infrared spectroscopic surveys (including 2MASS, UKIDSS, DENIS, MSX, GLIMPSE and WISE data). For the first time, 14 early-type stars including one Wolf-Rayet star and 4 O4-7 stars were detected in the whole W33 complex, and one Oe star in W33-Main. This star population, combined with the non-detection of red supergiants indicates a ~2–4 Myr age range for these stars. Then, Kohno et al. (2018) and Dewangan et al. (2020) used a combination of large-scale observations to highlight the presence of at least two populations of massive stars either recently formed or currently being formed. They both formulated the assumption that a cloud-cloud collision might have triggered star formation in the complex. Analysing the kinematics of the region over tens of parsecs, Liu et al. (2021) also concluded that gas flows along filaments might trigger star formation in W33. More recently, Murase et al. (2022) and Tursun et al. (2022) observed emission from a handful of NH₃ lines. They both inferred rotational temperatures from the (1,1) and (2,2) pair in comparable sub-fields of the global W33 complex, measuring values of 16–26 K for the former and 14–32 K for the latter. Their results were consistent given the slightly different fields observed, the different angular resolutions, and also the different formulas used to constrain their values. The former interpreted these high values by means of the feedback exerted by the massive stars in the form of the compact H II region in W33-Main. Beilis et al. (2022) identified three ultra compact H II (hereafter UCH II) regions, using the [Ne II] 12.8 μm emission line. Furthermore, they posited that each of these UCH II regions holds multiple, relatively moderate-mass

OB stars. Finally, Khan et al. (2022) confirmed the presence of three UCH II regions and characterised them as 'evolved' (with the same 2–4 Myr age as constrained by Messineo et al. 2015) and 'in expansion' through GHz observations of line and continuum emission.

3. Observations and data reduction

3.1. The G012.80 protocluster in the ALMA-IMF Large Programme

Between December 2017 and December 2018, as part of the ALMA-IMF² Large Programme (project #2017.1.01355.L; PIs: Motte, Ginsburg, Louvet, Sanhueza, see M22), 15 of the most massive protoclusters located at a distance between 2 and 6 kiloparsecs from the Sun were observed. Both the 12 m and 7 m antennas of the interferometer were used in Bands 3 and 6, respectively, at 3 mm and 1.3 mm, or ~100.6 GHz and ~228.9 GHz. The W33- on the 18^h14^m13^s.370, -17°55'45"200 [J2000] position. Around this position, mosaics were performed by the ALMA 12 m and 7 m arrays, respectively composed of 67 (12 m) and 27 (7 m) pointings at 1.3 mm and 13 (12 m) and 5 (7 m) pointings at 3 mm. Details on the mosaics and synthetic beamsizes are reported in Table 1. A finder's chart of the whole W33 complex and of the location of our observed field can be found in Fig. 1. The angular resolution is of the order of 1'', enabling the detection of structures of 2400 au in size. For the 12 m data, the maximum recoverable scales are ~6.6'' at 1.3 mm and ~9.9'' at 3 mm (respectively 0.8 and 1.1 pc), enabling us to detect filaments and H II regions over the observed mosaic.

A total of four and eight spectral windows (spw) were set up in Bands 3 and 6, respectively, for total bandwidths of respectively 3.7 GHz and 2.9 GHz, respectively. Within the ALMA-IMF consortium, we re-divided these spectral windows into smaller ones centred on individual lines from prominent molecules. Overall, we list all the spectral windows that we used in Table 1. This table also summarises other relevant information for our observations. A more complete description of the entire datasets of the ALMA-IMF Large Programme can be found in M22, G22, and C23.

3.2. Data reduction

The W33-Main data that we used correspond to the continuum images and line cubes delivered by G22 and C23, respectively. The ALMA consortium corrected these data for system temperature and spectral normalisation following the problems detected in data from cycles 3 to 7³. As reported in G22, these corrections were not significant with regard to continuum data, but they are crucial for lines' data. An automatic CASA 6.2 pipeline⁴ developed by the ALMA-IMF consortium and fully described in G22 was used to produce two continuum (at 1.3 and 3 mm) and two corresponding spectral-window images. The cleaning was done using the TCLEAN task of CASA. The use of the multi-scale option as well as the use of a continuum start model on the cubes improved the cleaning, especially on the extended emission. To avoid any divergence issues on the brightest lines, a cleaning

² ALMA project #2017.1.01355.L, see <http://www.almaimf.com>

³ ALMA ticket: <https://help.almascience.org/kb/articles/607>, <https://almascience.nao.ac.jp/news/amplitude-calibration-issue-affecting-some-alm-a-data>

⁴ ALMA Pipeline Team, 2017, ALMA Science Pipeline User's Guide, ALMA Doc 6.13.

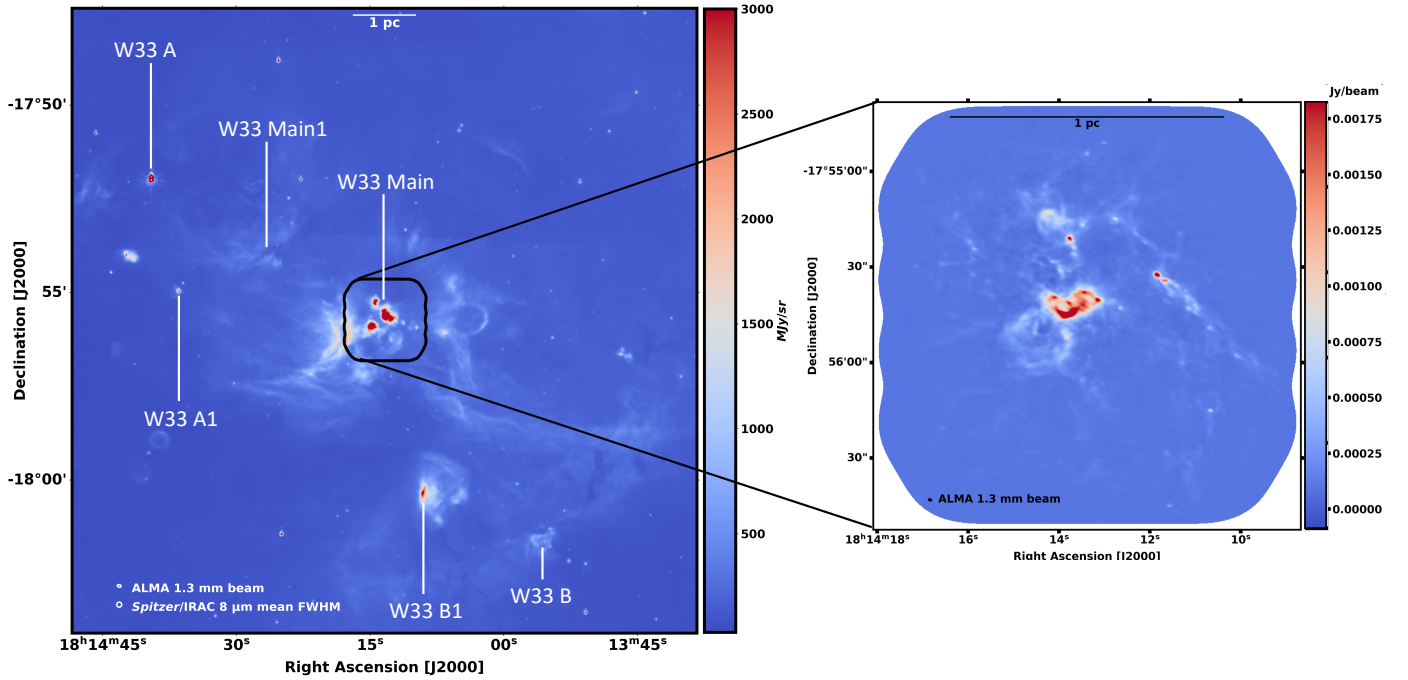


Fig. 1. Overview of W33 complex and W33-Main. *Left:* overview of W33 region seen in the 8 μm channel of the *Spitzer* telescope (with labels from Immer et al. 2014) with a 2'' resolution and comprised of W33-Main, A, B, A1, B1, and Main 1. *Right:* zoomed-in view of W33-Main as observed by the ALMA-IMF large programme in continuum at 1.3 mm.

Table 1. Observational properties of W33-Main region as imaged by ALMA-IMF and the principal lines of interest.

ALMA band	Pointings 7 m 12 m	Mosaic size ("×")	$\Theta_{\text{maj}} \times \Theta_{\text{min}}^{(a)}$ ("×")	Configuration
B6 (1.3 mm)	27 67	132 × 132	1.1 × 0.7	TM1; C43-2, 7M
B3 (3 mm)	5 13	190 × 180	1.4 × 1.2	TM2; C43-4, TM1; C43-1, 7M ^(b)
B6 spw name	Central frequency (GHz)	Lines	Bandwidth (MHz)	Resolution (MHz)
1	217.15	SiO(5–4)	234.38	0.282
5	230.53	CO(2–1)	468.75	0.969
7	232.45	continuum	1875.00	1.129
B3 spw name	Central frequency (GHz)	Lines	Nandwidth (MHz)	Resolution (MHz)
0	93.17	N ₂ H ⁺ ($v = 0, J = (1-0)$)	117.19	0.0706
1	92.034	H41 α	105.454	0.564
1	92.076 ^(c)	C41 α –He41 α	35.532	0.564
1	92.20	continuum	937.50	0.564
2	102.60	continuum	937.50	0.564
3	105.00	continuum 2	937.50	0.564

Notes. ^(a)Major and minor sizes of the beam at half maximum. Θ_{beam} is the geometrical average of these two quantities. ^(b)The long- and short-baseline observations are denoted TM1 and TM2, respectively. C43-2, C43-4, C43-1, and 7M refer to the observation time using, respectively, the 12 m (42 antennas) and 7 m (10 antennas) antennas. ^(c) Value chosen in the middle of He41 α and C41 α non-spectrally resolved lines, respectively, at 92.07 GHz and 92.08 GHz.

threshold of 5σ (with $1\sigma = 0.20 \text{ mJy beam}^{-1}$ at 1.3 mm and $1\sigma = 0.26 \text{ mJy beam}^{-1}$ at 3 mm) was set for the entire spectral windows for both bands. Finally, because of the extended emission in this field, self-calibration of the data was necessary to achieve the requested sensitivity for continuum images. Complete information about the self-calibration of the data can be found in G22. This calibration phase resulted in a significant noise reduction of up to $\sim 46\%$, for Band 3.

Using this procedure, two types of continuum images per band were produced by the ALMA-IMF reduction team. The first one is called *bsens*, meaning ‘best sensitivity’, and it encompasses all spectral windows with the contribution of both continuum and line emission. It provides the best sensitivity, allowing the detection of cores with masses down to $\sim 2 M_{\odot}$ at 5σ . The second type of continuum image produced by the pipeline is called the *cCleanest* map. Its purpose is to estimate

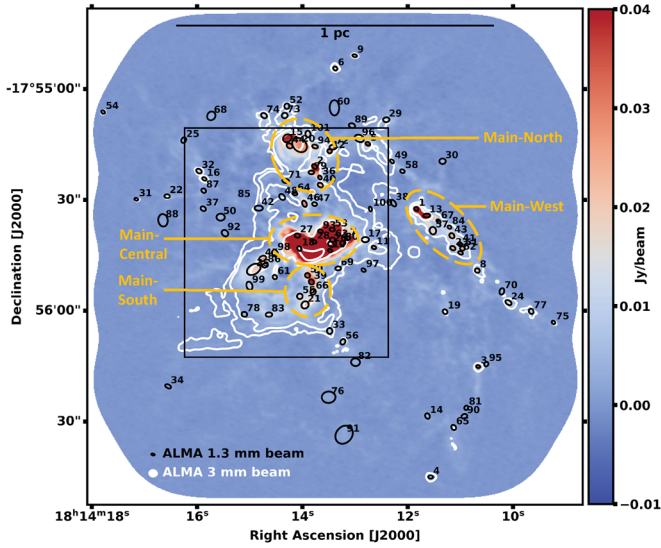


Fig. 2. bsens continuum emission maps of ALMA-IMF field for W33-Main at 1.3 mm in colours and at 3 mm in white contours (with levels at 4, 12, 200, 800 σ with $1\sigma = 0.26$ mJy beam $^{-1}$). All compact sources identified by *getsf* are outlined by black ellipses. The sub-regions identified by I14 are indicated by yellow-dashed ellipses (see text for details). The synthesised beams are shown in the lower left corner, and in the upper part, a 1 pc scale is shown.

the contribution from only the continuum, cleaned as much as possible from line contamination. Using the `Find_Continuum` routine developed by Todd Hunter⁵, we removed channels contaminated by line emission. To produce these maps for the W33-Main field, more than 80% of the continuum bandwidth was used (see G22).

Finally, in addition to the continuum maps and in order to study chemical properties among these regions, emission maps from the most prominent spectral lines of each band was cleaned with a version of the ALMA-IMF pipeline adapted for line cubes (see C23). These include CO (2–1) and SiO (5–4) in Band 6, later used for outflow identification; N₂H⁺ (1–0) in Band 3, later used to study the filamentary structure of the region; and H41 α and {He41 α + C41 α } in Band 3, later used to study the free-free emission (see specifications in Table 1).

3.3. Large-scale structures seen in continuum emission

Figure 2 shows an overlay of the two bsens maps of the continuum emission at 1.3 and 3 mm, with the candidate compact continuum sources (see Sect. 4.1). Several prominent features can be seen in this figure. They correspond to the ‘sources’ identified by I14 based on continuum observations at 2.5'' resolution and are called Main-South, Main-Central, Main-North, and Main-West (see Fig. 2). The better resolution and sensitivity achieved with ALMA allowed us to probe the nature of these structures in more depth. The Main-Central, Main-South, and Main-North structures are reminiscent of bubbles already identified in the region by past studies with other tracers, the walls of which seem to be traced by continuum emission at 1.3 and 3 mm. The Main-West structure appears to be a filament. Additional fainter filamentary structures appear on our map, mostly in the south-western quadrant of W33-Main. Finally, a small additional bright structure also shows up in the northeastern direction

⁵ <https://safe.nrao.edu/wiki/bin/view/Main/CasaExtensions>

from Main-North. At the wavelengths we observed, especially at 3 mm, the continuum emission is a combination of dust emission with free-free emission. The nature of these structures is determined below.

3.4. Dynamical structures

In order to understand the nature of the structures described above, we first used maps of the emission from selected lines. Figure 3 shows the bsens continuum map at 1.3 mm, overlaid with line emission maps of ¹²CO (2–1) in panel a), SiO (5–4) in panel b), and N₂H⁺ (1–0) in panel c). These maps trace the dynamical structures in the region: filaments and bipolar outflows.

The ¹²CO emission is of complex shape and structure. The analysis of the gas at rest/ambient velocities is irrelevant since this line is riddled with self-absorption. Blueshifted and redshifted emission can be seen. Such emissions are often correlated, indicative of the presence of bipolar outflows from protostellar cores (see Sect. 5.2). On the other hand, the SiO (5–4) line emission at ambient velocities correlates with structures seen in the continuum emission likely associated with dust structures, as in Main-West. In such regions, low-velocity shocks propagating in a dense medium could generate a somewhat higher abundance and/or excitation of SiO than in other parts of the cloud. This kind of emission was, for instance, already reported and interpreted in the W43-MM1 filament by Nguyen Luong et al. (2013) and Louvet et al. (2016). The ambient emission of SiO traces the additional component in the southwestern quadrant, already hinted at in the 1.3 mm map and with a 8 μ m counterpart. This component is very elongated, even collimated; it is not clearly detected in ¹²CO and is faint in the continuum map at 1.3 and even fainter at 3 mm. Higher velocity, blueshifted and redshifted SiO (5–4) emission is also detected, not only from well-identified bipolar outflows (see Sect. 5.2).

Contrary to ¹²CO and SiO lines, the N₂H⁺ (1–0) line is brighter at ambient velocity than in the blueshifted and redshifted velocity ranges. This is because this line traces the dense medium (Pety et al. 2017), including filaments. Figure 3c confirms the filamentary nature of the Main-West (I14) structure and reveals the existence of multiple, extended filaments within W33-Main. One in the northwestern direction from the Main-Central structure, a few in the north direction from it, one filament extending south from it, and finally two branches extending south from the Main-West filament. One of these two branches is the one seen in SiO line emission. Most of the filaments we detected in N₂H⁺ were also detected in DCN (3–2) by C23, except for this branch seen in SiO. A complete analysis of these filamentary emissions is beyond the scope of our study, but it will be the subject of a forthcoming publication (Salinas et al., in prep.). Overall, the presence of bipolar outflows seen in CO and SiO is a sign that protostellar sources are present in the region, suggesting that W33-Main is an evolved region in the sense defined by M22. In addition, the presence of multiple and extended filaments has been found to also be a signature of evolved regions within the ALMA IMF sample by C23.

3.5. H II regions

The ALMA-IMF dataset also enables us to recognise the presence H II regions. Figure 4a shows the bsens continuum map at 3 mm, overlaid with i) the H41 α emission map at 92.03 GHz, integrated between -5.8 and 84.4 km s $^{-1}$ (Galván-Madrid et al. 2024); and ii) the Ne II ²P_{1/2}–²P_{3/2} emission at 12.81 μ m

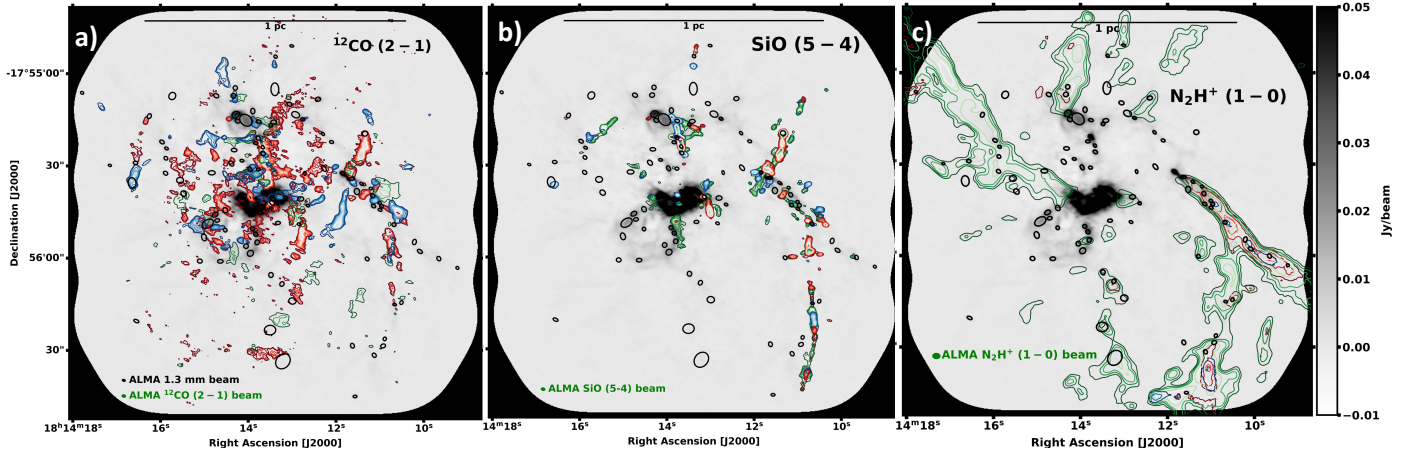


Fig. 3. bsens continuum map at 1.3 mm as background image in shades of grey with coloured contours of moment 0 of ^{12}CO (2–1) line emission in *panel a*, SiO (5–4) line emission in *panel b*, and N_2H^+ (1–0) line emission in *panel c*. For all three panels, the synthesized beams are presented in the lower left corners and a 1 pc scale-bar is shown in the upper part of the maps. Blue, green, and red correspond to integration between respectively, [12; 32] km s^{-1} , [32; 42] km s^{-1} , and [42; 62] km s^{-1} for all three molecules. (a) With $1\sigma = 0.7 \text{ Jy beam}^{-1} \text{ km s}^{-1}$, the blue and red contour levels are 4, 6, 8, 10, 12, 14 and 16σ . The green ones correspond to 2, 3, 4, and 5σ . (b) $1\sigma = 0.03 \text{ Jy beam}^{-1} \text{ km s}^{-1}$ and the corresponding contours for all colours are 3, 7, 10, 13, 15, and 17σ . (c) For all colours, the integration levels are 10, 15, 20, 30, and 40σ with $1\sigma = 0.05 \text{ Jy beam}^{-1} \text{ km s}^{-1}$. We show the *getsf* compact sources in black ellipses.

presented by Beilis et al. (2022). Figure 4b shows the bsens continuum map at 1.3 mm, overlaid with selected contours of the same $\text{H}41\alpha$ and $\text{Ne II } ^2\text{P}_{1/2}-^2\text{P}_{3/2}$ emission maps. We did not detect any $\text{H}41\alpha$ emission outside these zoomed-in images, which confirms the dusty nature of the filament branches extending the Main-West region. Within the zoomed-in images, we found a broad correlation of the $\text{H}41\alpha$ emission with the 3 and 1.3 mm continuum emission on the one hand and the Ne II emission on the other. We were also able to identify the structures listed by I14: the shell corresponding to Main-Central delimits an H II region, the Main-South structure seems to be associated with the cavity walls of another H II region, and the structure seen to the north-east of Main-North is also an H II region. Using these two species, we were finally able to define three types of regions in the global W33-Main observed by ALMA-IMF. First, we defined everything that lies within the 5σ contours of the $\text{H}41\alpha$ emission (Fig. 4b) as ‘ H II regions’. We found three of these structures, which are tagged in Fig. 4b following the classification of Beilis et al. (2022). Then, we defined the regions that lie i) between 1σ (Fig. 4b) and 5σ contours of the $\text{H}41\alpha$ emission and ii) between 1σ and 5σ contours of the Ne II emission (Fig. 4b), and iii) outside of our ‘ H II regions’ as ‘ H II region surroundings’, a zone of lower free-free contamination. Finally, outside these σ contours, we defined ‘the rest of the cloud’ without significant influence of free-free emission. The extent and brightness of H II regions within a given ALMA-IMF field was measured by M22 through the $\sum_{\text{H}41\alpha}^{\text{free-free}}$ parameter (see their Table 4). For W33, M22 found a value of 7 Jy pc^{-2} , which contributed to putting W33-Main in the category of ‘evolved regions’ within the programme.

4. Identification of cores

We extracted compact continuum sources from the maps introduced in Sect. 3.2, with the aim of building a catalogue of prestellar and protostellar cores with their basic properties (position, size, masses). Below, we present our criteria for the exclusion sources for which the emission does not originate from

thermal dust emission, as well as our method to evaluate the fraction of the flux that comes from dust grains for sources whose emission is contaminated by free-free emission.

4.1. Extraction of compact sources

We used the *getsf* (Men’schikov 2021b) extraction tools to identify compact continuum sources in our dataset. The multi-scale source and filament extraction method *getsf* (Men’schikov 2021b) separates the source-like peaks from their backgrounds using spatial decomposition before extracting sources. Its benchmarking including detection completeness and measurement accuracy on simulated images can be found in Men’schikov (2021a). We adopted the *getsf* definition of sources; they are the relatively round emission peaks that are significantly stronger than the local surrounding fluctuations (of background and noise), indicating the presence of the physical objects in space that produced the observed emission. If a structure is too elongated or has a very complex shape, it is unlikely to be a compact core. The single user-definable parameter of *getsf*, that is, the maximum size of the sources of interest, is set to three times the beam size (geometric average of its major and minor extents) in each of the images.

As it is the image with the best sensitivity and resolution and the least contamination by free-free emission, we used the 1.3 mm bsens 12 m array image, uncorrected for primary beam effects for the detection of compact continuum sources. We then used the primary-beam-corrected version of this image to measure the cores’ sizes and estimate their fluxes. In addition, the primary-beam-corrected 3 mm bsens and 1.3 and 3 mm cleanest images were used to perform size estimates and flux measurements. After running *getsf*, we obtained a first catalogue of 101 sources. Figures 2 and 3 locate the sources of the catalogue thus obtained.

In the first catalogue of sources obtained with the *getsf* method and in line with what was done by Pouteau et al. (2022), compact sources for which i) the goodness and significance factor (defined in Men’schikov 2021b) are less than 1,

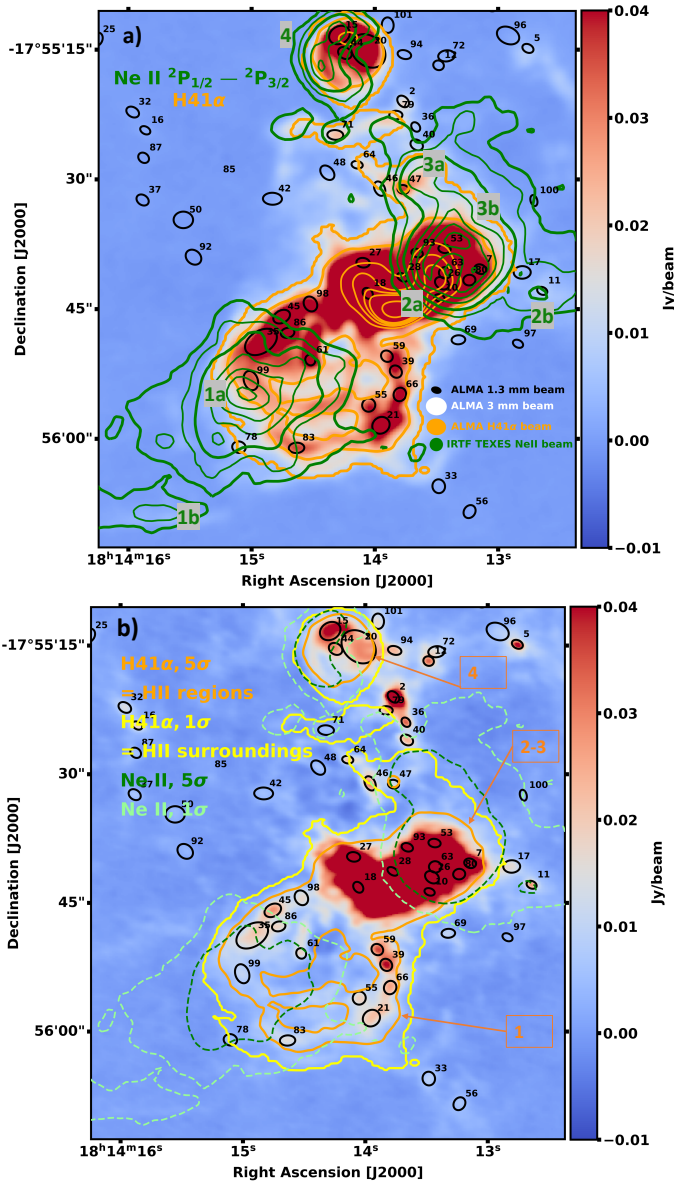


Fig. 4. Zoomed-in view of black rectangle shown in Fig. 2. *Panel a:* bsens continuum map at 3 mm. The orange contours show the H41 α line emission (see Galván-Madrid et al. 2024) with levels of 1, 5, 20, 30, 40, 50, and 100 σ ($1\sigma = 0.01$ Jy beam $^{-1}$). The green contours are the Ne II line emission with the labels of Beilis et al. (2022). The contour levels are 1, 2, 5, 10, 15, 20, and 25 σ ($1\sigma = 0.002$ erg s $^{-1}$ cm $^{-2}$ sr $^{-1}$). *Panel b:* yellow and orange contours, on top of the bsens continuum map at 1.3 mm, show the H41 α line emission with levels of, respectively, 1 and 5 σ ($1\sigma = 0.01$ Jy beam $^{-1}$). The orange contours define the H II regions, labelled with numbers, and the yellow contours define the surroundings of these bubbles. The dashed pale green and dark green contours are the Ne II line emission, corresponding to contour levels of 1 and 5 σ , respectively ($1\sigma = 0.002$ erg s $^{-1}$ cm $^{-2}$ sr $^{-1}$).

or ii) $S^{\text{peak}} \leq 2\sigma^{\text{peak}}$ or $S^{\text{int}} \leq 2\sigma^{\text{int}}$ ⁶, or iii) there is a too high ellipticity ($a/b \leq 2$, with a the major axis and b the minor axis), were removed. After application of these criteria, the filtered *getsf* catalogue contains 94 sources. We note that for 30 out of these 94 sources (which makes about 1/3 of the global sample),

⁶ S^{peak} and σ^{peak} are, respectively, the peak flux and the associated error of each core in Jansky beam $^{-1}$. S^{int} and σ^{int} correspond to the integrated flux and its error on the size of each sources in Jansky.

we only have upper limits at 3 mm ($S_{3\text{ mm}}^{\text{int}} \leq 1\sigma_{3\text{ mm}}^{\text{int}}$). These 94 sources, as well as their position, size, position angle, and peak and integrated fluxes with associated uncertainties at 1.3 and 3 mm are listed in Table B.1. In the following, we refer to this catalogue as ‘the *getsf* filtered catalogue’, although further classifications will be applied to it. Following the work done by Pouteau et al. (2022), we also used the *Gext2D* method and found that more than 75% of the sources have a match with those extracted by *getsf* (in terms of the cores’ positions, sizes and fluxes; see Table B.1).

We estimated the completeness level of the *getsf* core catalogue. To this aim, a background bsens image of W33-Main at 1.3 mm was produced by *getsf* by replacing each compact source identified with an average of the surrounding emission. We then injected ~ 800 synthetic sources over this background image. These synthetic sources were split into ten bins of mass, logarithmically spaced between 0.15 and 3.0 M_{\odot} . We chose a Gaussian flux density profile for these synthetic sources, equal to the median size of extracted sources (FWHM of 1.3'' i.e. 3000 au at 2.4 kpc). Sources were randomly injected in a regular grid, not allowing cores to overlap. We performed five series of completeness simulations, varying the location of synthetic sources to dilute the effects of the chosen grid and to allow us to estimate the error bars. We ran the extraction algorithm *getsf* on all these synthetic images with the same parameter as for the observations. To estimate a global 90% completeness level, we compared the mass and location of injected sources that were thus detected by *getsf* with the mass and location of injected sources. We found that above $\sim 1.0 \pm 0.2 M_{\odot}$ for this *getsf* core catalogue, we recovered 90% of the sources (see Fig. B.1). Overall, 72% of the sample of Table B.1 lie above this completeness level.

4.2. Free-free contamination

The presence in our maps of the three H II regions described in Sect. 3.5 raises a doubt about the origin of the continuum emission at 1.3 mm, and even more at 3 mm, and hence on the nature of the compact sources we detected within these structures. Indeed, the emission at these wavelengths can originate from a combination of dust continuum and free-free mechanisms. First, we removed the compact sources whose emission is completely attributable to free-free emission from our core catalogues, and then we subtracted the contribution of free-free emission from the measured flux density originating from each core located in a potentially ionised region. This is because our aim is to measure the mass of individual cores based on the flux densities only coming from the dust continuum at 1.3 mm. These two tasks require us i) to identify the cores located in partially or fully ionised regions and ii) to estimate the contribution of the free-free emission for these cores.

In order to achieve our first objective, we compared our *getsf* filtered catalogue with the H41 α emission, the He41 α + C41 α , and Ne II $^2P_{1/2}$ – $^2P_{3/2}$ emission (see Fig. 5). We considered that the continuum emission of the cores located within 1 σ contours of H41 α or Ne II is likely to be at least contaminated by free-free emission. We identified 35 such sources from our *getsf* filtered catalogue. We then overlaid our *getsf* filtered catalogue on a spectral index map. That map was built from Band 3 and 6 continuum maps at their minimum common beam (Díaz-González et al. 2023; see their Eq. (2)). The ALMA-IMF maps were merged with the pilot of the Mustang-2 Galactic Plane Survey (MGPS90; Ginsburg et al. 2020) at 3 mm; and the Bolocam Galactic Plane Survey (BGPS; Aguirre et al. 2011 and Ginsburg et al. 2013) at 1.3 mm. Figure 5c separates the regions where the

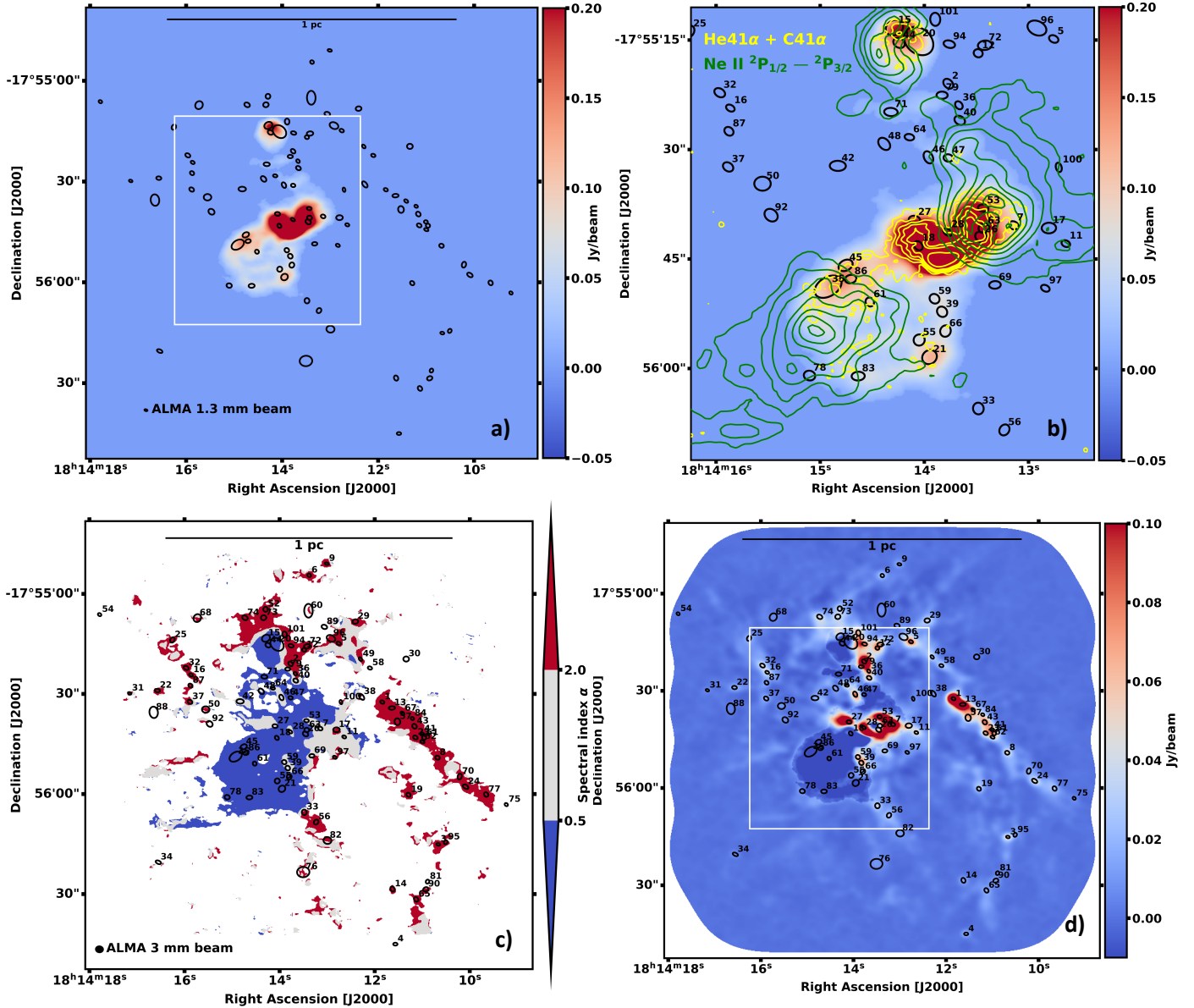


Fig. 5. Study of the free-free contamination within W33-Main. *Panel a:* H41 α line emission map at 92.034 GHz integrated between -5.8 and 84.4 km s $^{-1}$ (see Galván-Madrid et al. 2024), with the sources identified by *gatsf* in black ellipses. *Panel b:* zoomed-in view of H41 α line emission map in white rectangle in panel a. The yellow contours show He4I α and C4I α lines' emission maps at 92.072 and 92.080 GHz, respectively, regridded to the bsens 1.3 mm continuum spatial resolution, with contour levels of 3, 6, 9, 13, 16, and 30σ ($1\sigma = 0.064$ Jy beam $^{-1}$). The green contours are the Ne II line emission with contour levels of 1, 2, 3, 4, and 5σ ($1\sigma = 0.01$ erg s $^{-1}$ cm $^{-2}$ sr $^{-1}$). *Panel c:* spectral index α map with the following mask: if $\alpha \leq 0.5$ the emission is free-free dominated (in blue), if $\alpha \geq 2$ the emission is dust dominated (in red), and in between ($0.5 \leq \alpha \leq 2$) we call the emission 'free-free contaminated' (in grey). *Panel d:* cleanest continuum map at 1.3 mm from which the free-free estimated contribution at 1.3 mm was removed using the H41 α line and assuming an optically thin spectral index ($\alpha = 0.1$). The resulting emission is equal to or less than zero if it is dominated by free-free emission (dark blue in the map). The map is shown at the 3 mm angular resolution.

3 mm emission is above 3σ in three regions depending on the spectral index value. Below 0.5 is where the 1.3 mm emission is expected to be dominated by the free-free emission. Between 0.5 and 2.0 is where it should be contaminated by the free-free emission. Finally above 2.0 it should be dominated by dust emission. At this stage, we found that 17 cores are located inside the free-free-dominated parts and 18 are inside the contaminated parts of the map, recovering the 35 sources listed based on line emission.

We sought an ultimate confirmation as well as a means to evaluate the dust continuum emission at 1.3 mm for the cores

located in free-free contaminated, and even, if possible for those located in the free-free dominated parts of the region. To this aim, we generated a map of the 1.3 mm 'pure' dust emission by subtracting the contribution from the free-free emission at 1.3 mm from the cleanest map at 1.3 mm. The contribution from the free-free to the continuum emission at 92.034 GHz was first estimated using the H41 α recombination line under the LTE assumption and then extrapolated to a 1.3 mm wavelength using an optically thin emission of $I_{\text{ff},\nu} \propto \nu^{-0.1}$. Galván-Madrid et al. (2024) provides the details on how such calculations were used to produce pure dust-, free-free-subtracted maps of

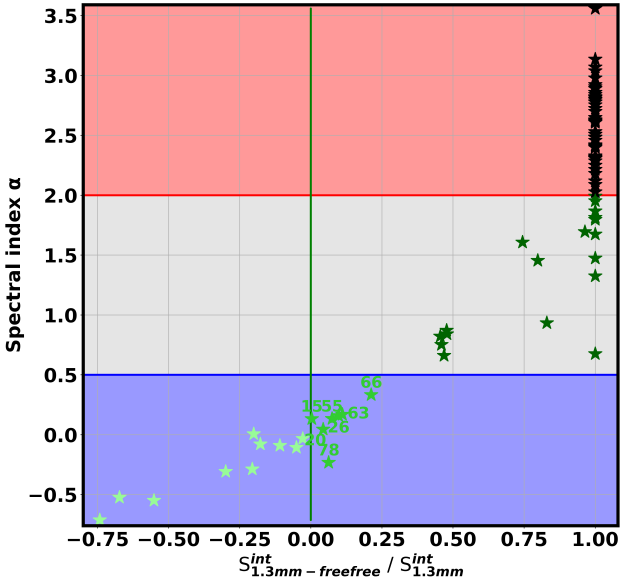


Fig. 6. Cross-correlation between spectral index measurements displayed in Fig. 5c (y-axis) and ratio of the flux density from ‘pure’ dust emission over the bsens 1.3 mm flux density at 3 mm angular resolution for each core from the *getsf* filtered catalogue (x-axis). The x-axis shows the percentage of 1.3 mm emission due to dust emission at 3 mm angular resolution. Free-free contaminated cores are shown in dark green, free-free dominated cores in light green, and ‘uncertain’ ones (see Sect. 4.2) in neutral green, and the rest of the cores are shown in black.

continuum emission at 1.3 mm. Figure 5d shows the result of this subtraction, performed at the 3 mm angular resolution. In principle, this figure shows the distribution of the pure dust emission (where the signal is positive) that we will be able to use to perform our core mass estimates.

In order to cross-compare the result from this method with the spectral index measurements displayed in Fig. 5c, we plot the correlation between the spectral index values, and in Fig. 6 we show the ratio of the flux density from pure dust emission over the *cleanest* 1.3 mm flux density at 3 mm angular resolution. This ratio directly indicates our estimate for the contribution of the dust emission to the total flux density at 1.3 mm at the 3 mm angular resolution. In this plot, the black symbols are the dust-dominated cores. The 18 cores located in the free-free-contaminated region of Fig. 5c are the ones for which we can measure the pure dust emission based on the data from Fig. 5d. We will subsequently refer to these cores as free-free contaminated. We found ten cores for which the signal in Fig. 5d is negative. For these compact sources, all the methods presented in this section indicate that they are not cores, but probably local peaks of free-free emission. We call them free-free dominated and hence remove them from our final core catalogue. Finally, seven cores (#15, #20, #26, #55, #63, #66, and #78) correspond to a positive but low signal in Fig. 5d. A careful examination of Fig. 5d even showed that these seven cores are all located at the edge of ionised regions and that their spatial definition includes pixels with both free-free-dominated and free-free-contaminated or even dust-dominated emission. This means that the result from our last two methods is not consistent for these sources; their spectral index value suggests that they could be local knots of free-free emission, whereas the contribution of dust emission to the 1.3 mm continuum emission, though low, is not zero. We treat all these seven cores as potential cores and hereafter

referred to them as ‘uncertain’. This means that we estimate the pure dust emission from these cores from Fig. 5d, even though the contribution from their free-free emission to the total 1.3 mm flux density is significant.

Among the 94 *getsf* cores, we identified ten free-free-dominated cores (which in the following study are removed from our core catalogue), seven free-free-uncertain cores, and 18 free-free-contaminated cores. For the last two categories, we applied a correction to the measurement of their continuum flux density.

4.3. Line contamination

Our *getsf* catalogue of compact sources was produced based on our bsens maps at 1.3 mm. In these maps, the emission of the continuum and the line emission from the gas species from all spectral windows are mixed. This means that a local peak of line emission can be confused with a continuum emission core. Good examples can be seen in Figs. 3a and b, where some compact sources lie within bipolar outflow structures. This is confirmed in the [bsens – cleanest] map at 1.3 mm, where compact sources can be either a real core in the foreground or background of an outflow lobe, or an outflow knot. In order to distinguish among these possibilities, we subtracted the CO (2–1) line (the brightest line in our dataset) from the bsens map at 1.3 mm and performed a new *getsf* extraction on this specific data product using the same extraction parameter as described in Sect. 4.1. In this new extraction, we found eight sources of particular interest. On the one hand, four sources (#82, #88, #97, #100) were missing with respect to our initial *getsf* catalogue. These sources are hence very likely to be outflow knots whose emission at 1.3 mm is dominated by the CO line, and we hence removed them from our core list. On the other hand, four sources (#23, #30, #36, #40) were located within lobes of outflows but still picked up by the *getsf* run over the CO-subtracted bsens dataset. These four cores are likely real, but their emission is contaminated by CO (and other lines) coming from an outflow in the foreground or the background. We kept them within our core catalogue, but used the *cleanest* flux densities for the following study (see Sect. 6).

In summary, among the 94 sources of our *getsf* filtered catalogue, we removed 10 free-free dominated and 4 CO emission-dominated sources. We also used a flux density correction for 25 cores with free-free contamination, and for 4 cores with line contamination. Our final *getsf* catalogue hence contains 80 cores.

5. Nature of the cores

After identifying the cores, we attempted to estimate their evolutionary stage, with the aims of distinguishing prestellar from protostellar objects. First, we used archival observations in the mid-infrared and near-infrared ranges to identify the potential Class I, II, and older objects present in W33-Main. With the WISE and 2MASS all-sky surveys we found a clear association between our source #24 and a Class I source of the WISE catalogue, a possible association between our source #19 and a CH₃OH maser as well as two potential correlations with water masers (albeit with a less clear association). We also used *Spitzer*/IRAC data from the GLIMPSE survey to look for Classical T-Tauri (CTTS) and HAeBe stars, as well as Class I and Class II protostars, but did not find any clear association between the few sources we thus found with any core from our list. More details on these searches can be found in Appendix A. Then, we used our ALMA dataset to look for tracers of an evolved star

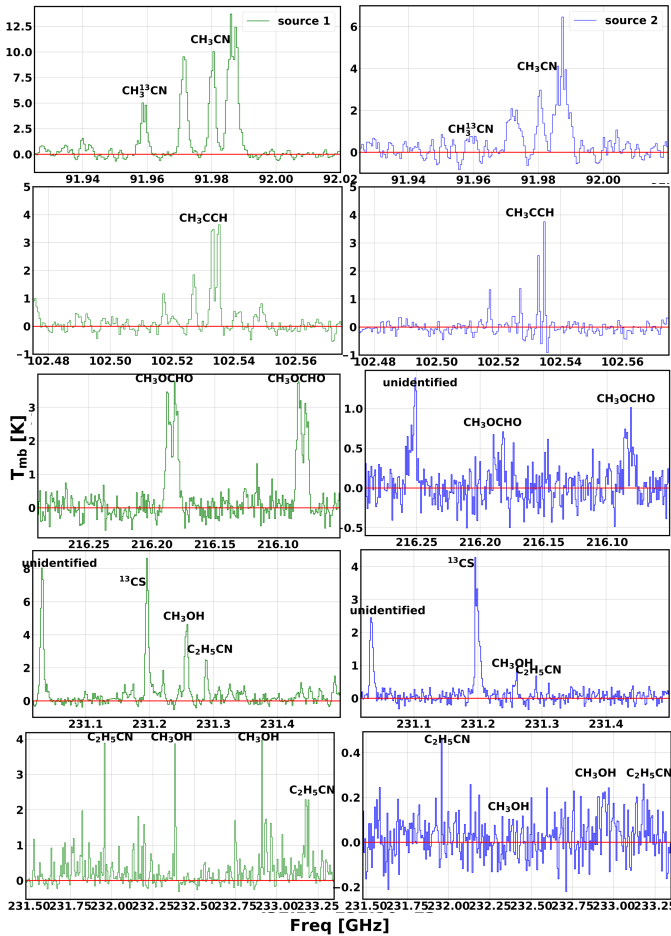


Fig. 7. Selected spectra from two hot core candidates, core #1 (*left panels*) and core #2 (*right panels*). From top to bottom, spectral windows 1 and 2 of Band 3 are shown, followed by spectral windows 0, 6, and 7 of Band 6. Source #1 is detected with many COMs lines. In all panels, the identified lines are indicated, and the baseline is shown with a red line.

formation stage. To do so, we first used the emission of selected lines from complex organic molecules to search for potential hot cores. We then used the CO and SiO emission lines (see Table 1) to detect potential outflows driven by the sources.

5.1. Identification of hot cores

We looked into whether some of the compact sources that we detected could be classified as hot cores, which would be a sufficient but not necessary condition to put them in the protostellar category. A hot core is usually defined as a compact (diameter ~ 1000 au) and hot ($T \geq 100$ K) region where a significant number of molecular lines from complex organic molecules (COMs) are detected (Herbst & van Dishoeck 2009). Indeed, COMs mainly form on grain surfaces through ice chemistry and are then released in the gas phase where the dust temperature becomes high enough. This typically occurs in protostellar environments.

In order to identify hot cores, an automatic search in methyl formate (CH_3OCHO) was performed by Bonfand et al. (2024) in all the fields observed by the ALMA-IMF program. This procedure provided a list of four hot core candidates in W33-Main. We independently followed the procedure described in Paper IV by Brouillet et al. (2022). Over the entire list of compact sources identified with *getsf*, we searched for 2σ detections of methyl

formate (CH_3OCHO , in spectral window 0 of Band 6), methyl cyanide (CH_3CN , in spectral window 1 of Band 3), methanol (CH_3OH , in spectral window 3 of Band 3 and spectral windows 6 and 7 of Band 6), propionitrile ($\text{C}_2\text{H}_5\text{CN}$, in spectral windows 6 and 7 of Band 6), and thioformaldehyde (H_2CS , in spectral window 3 of Band 3). We considered that the cores where at least three of these lines were simultaneously detected were hot-core candidates. We double checked that this classification was relevant by verifying that COMs' line forests were detected for these cores in spectral windows 6 and 7 of Band 6. This procedure led us to identify the same four hot core candidates towards sources #1, #2, #7, and #13.

Our clearest hot core case is source #1. We show a few selected spectral windows for this source in the left panels of Fig. 7. The hot core classification, however, can be as ambiguous as for source #2, for which the same spectra are displayed in the right panels of Fig. 7. We note that for these two cores, hints of a chemical differentiation can be seen; core #2 shows the same levels of emission in complex carbonated species such as CH_3CCH , but lower emission from oxygenated or N-bearing molecules.

5.2. Search for outflows

The presence of an outflow around a compact source is usually considered as a tracer of the presence of a protostellar object. Protostellar jets and outflows are usually detected in emission lines of abundant molecules such as CO and shock-tracing ones as SiO, on spatial scales up to approximately 1 pc, and over velocity ranges of up to ± 100 km s^{-1} from the velocity of the source (e.g. Snell et al. 1980, Frank et al. 2014). Here, we followed the same method as presented in, for example, Nony et al. (2023). We used the CO (2–1) and SiO (5–4) line emission to detect outflows, in the form of bipolar (blue/red) structures detectable in maps of intensity integrated over blueshifted and redshifted ranges of velocity. For both lines, we chose our velocity intervals for integration the following way: ± 5 km s^{-1} around $W33\text{-Main } v_{\text{lsr}} = 37$ km s^{-1} for the ‘ambient gas’ and $[12;32]$ km s^{-1} and $[42;62]$ km s^{-1} for the blueshifted and redshifted components.

We looked for outflows based on inspecting these maps shown in Fig. 3, consistently with what is done in all fields observed by ALMA-IMF in SiO (5–4) by Towner et al. (2024), and in CO(2–1) by Valeille-Manet et al., in prep. CO being self-absorbed around the rest velocity of the ambient gas, we removed this component prior to an inspection by eye. The cleanest case of outflow detection was when we were able to detect a blue and a red component surrounding a core, in both lines. We show an archetypal example for this situation, core #6, in Fig. 8. However, outflow structures are not always that easy to detect: their lobes can sometimes be aligned with the line of sight, they can be monopolar or multipolar, their association with a source can be ambiguous or confused by the coexistence of nearby cores, and their aspect might differ if we detect them in CO and/or in SiO. The outflow structures around core #7 epitomise our difficulties, as can be seen in Fig. 8. In order to confirm our detections, we hence used zoomed-in views of each tentative detection. We also generated and used complementary maps: moment 1 (central velocity in km/s) and moment 2 maps (velocity dispersion in km/s) and SO integrated intensity maps; and we produced PV-diagrams to confirm or infirm our detections. Following this procedure, we found 20 cores with outflows, nine of which are monopolar, nine bipolar, and two multipolar (associated with sources #7 and #8). Our four hot-core candidates

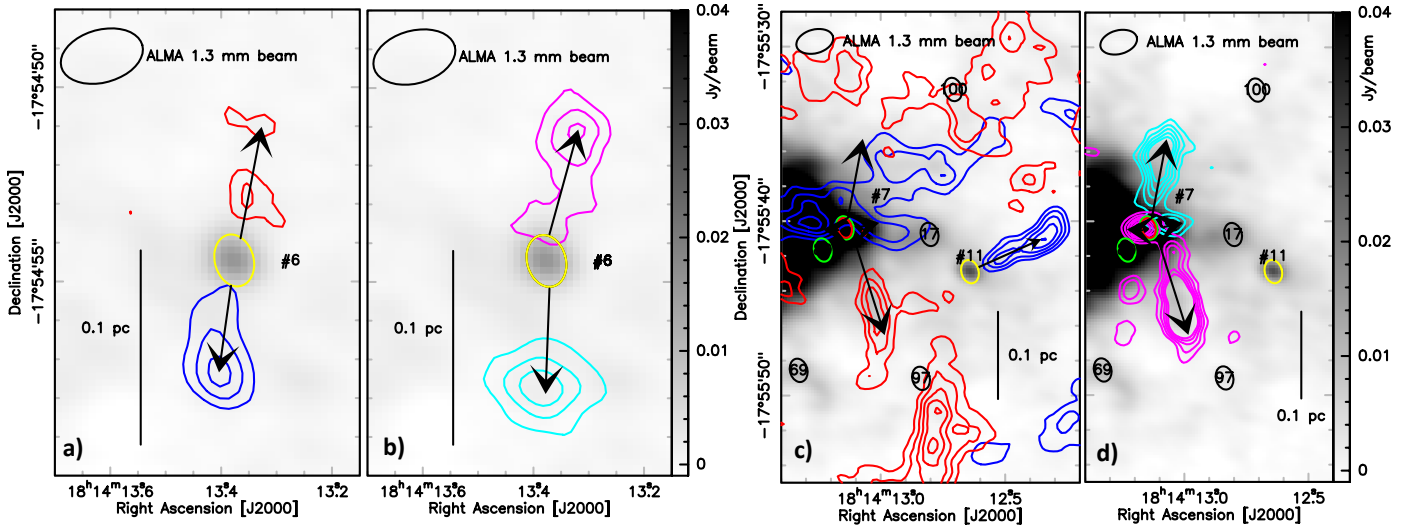


Fig. 8. bsens continuum map at 1.3 mm with coloured contours of moment 0 of ^{12}CO (2–1) in red and blue (*panels a* and *c*) and SiO (5–4) in magenta and cyan (*panels b* and *d*). For all four panels, the synthesised beams are presented in the upper left corners and a 0.1 pc scale bar is shown. Blue (cyan) and red (magenta) correspond to integration between, respectively, [12; 32] km s^{-1} and [42; 62] km s^{-1} for the two molecules of study. *Panels a* and *c*: with $1\sigma = 0.7 \text{ Jy beam}^{-1} \text{ km s}^{-1}$, blue and red contour levels are 4, 6, 8, 10, 12, and 14σ . *Panels b* and *d*: $1\sigma = 0.03 \text{ Jy beam}^{-1} \text{ km s}^{-1}$ and the corresponding cyan and magenta contours are 3, 7, 10, 13, 15, and 17σ . In coloured markers, the *getsf* cores are shown with ellipses: hot core candidates in red (see Sect. 5.1), cores associated with outflows in yellow, free-free contaminated and uncertain ones in green, and prestellar ones in black following scenario A (see text, Sect. 5.2).

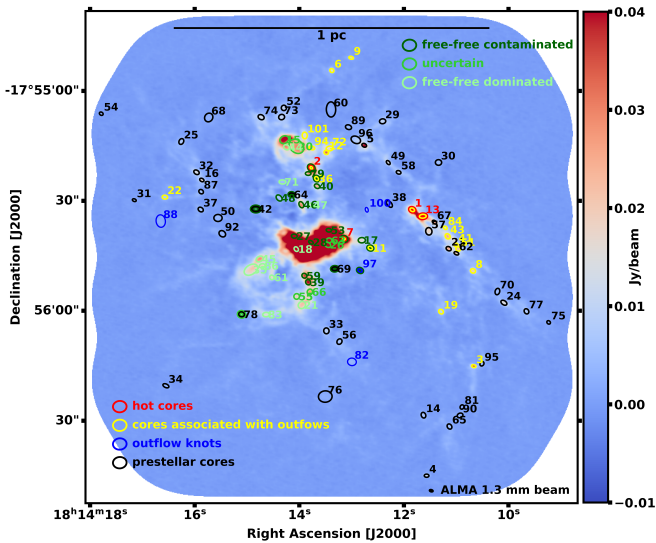


Fig. 9. bsens continuum map at 1.3 mm obtained with ALMA, with cores from the *getsf* filtered core catalogue. The colours now represent the different categories of cores that we identified: free-free contaminated cores in dark green, free-free dominated cores in light green, and ‘uncertain’ cores (see Sect. 4.2) in neutral green. Outflow knots/CO-contaminated cores (see Sect. 4.3) are shown in blue, hot core candidates (see Sect. 5.1) in red, cores associated with outflows (see Sect. 5.2) in yellow, and the remaining prestellar cores in black, following scenario A (see text, Sect. 5.2).

belong to this list, and so does the CH_3OH maser identified by Messineo et al. (2015) (core #19). On the contrary, the water masers detected by Messineo et al. (2015) do not seem to be associated with any outflow. We explicitly mentioned the association of a given core with an outflow in Table B.1. In the following developments, we consider that these cores are of protostellar nature (Fig. 9). Finally, we note that core #24 has no associated

outflow, but it is identified as a Class I source using the WISE catalogue. We retained the ‘protostellar’ classification for this core. The total number of protostellar cores at this stage is hence 21, and this number is not modified by the GLIMPSE analysis (see discussion in Appendix A).

Our search for outflows was particularly difficult in the H II regions and their surroundings (see Sect. 3.5), where there is little SiO emission, and where blueshifted and redshifted structures in CO are often confused. It is hence very difficult to rule about the nature of the cores for the majority of the seven uncertain and 18 free-free-contaminated cores we identified in Sect. 4.2. From the uncertain list, core #78 is clearly not associated with an outflow. From the contaminated list, core #97 was removed from the list of cores as we found that it was an outflow knot (see Sect. 4.3); three are clearly not associated with an outflow (#42, #64, #69), and four were already clearly associated with an outflow (#2, #7, #11, #36). This left us with 6 + 10 cores for which a potential association with outflow activity was unclear. We hence decided to study two scenarios; in scenario A, only the 21 cores mentioned in the previous paragraph are considered protostellar (26% of the sample) and the 59 others are prestellar. In scenario B, the 6+10 cores mentioned above are added to the list of protostellar ones, resulting in 37 protostellar cores (46% of the sample) and 43 prestellar ones. Figure 9 illustrates our findings on the nature of cores in W33-Main.

6. The global core mass function in W33-Main

In order to build a global core mass function in W33-Main, we first estimated the dust temperature down to core scales over the observed field, and we then computed individual cores’ masses.

6.1. The dust temperature in W33-Main

We estimated the dust temperature in W33-Main using the Point Process MAPPING procedure (hereafter PPMAP,

Marsh et al. 2015). PPMAP is a so-called resolution-enhancing method aimed at producing maps of column density and the temperature of a region observed at various wavelengths from the mid-infrared to the millimetre range. In this Bayesian procedure, the spectral energy distribution from the dust emission is described by a combination of modified blackbody functions at given temperatures and given spectral emissivity indices. The priors can be the temperature of the medium, the index of the opacity law β , and a dilution factor η . The latter represents the degree to which the procedure is forced to represent the data with the least number of building blocks of the system, which are characterised by three parameters: the 2D position projected on the plane of the sky (x, y) and the dust temperature T . The resulting product is a hypercube of column density as a function of dust temperature, which we used to produce a single map of column-density-weighted dust temperature.

The systematic application of PPMAP to regions observed by the ALMA-IMF programme is ongoing and is the object of Dell’Ova et al. (2024). In their products that we used here, a flat prior was used for $\log(T)$, and a fixed value of 1.8 was used for the spectral emissivity index prior (Planck Collaboration XXIV 2011; Planck Collaboration Int. XVII. 2014; Planck Collaboration XII 2014), on which an uncertainty of ± 0.2 was explored. Additionally, a value of $\kappa_{300} = 0.1 \text{ cm}^2 \text{ g}^{-1}$ for the dust opacity per unit (gas + dust) at $300 \mu\text{m}$ was adopted. Eight individual maps were used: two APEX observations (the ATLASGAL one at $870 \mu\text{m}$ with the LABOCA receiver see Schuller et al. 2009 and Csengeri et al. 2014 and one at $350 \mu\text{m}$ with the SABOCA receiver see Lin et al. 2019); three Hi-GAL (*Herschel*, PACS, and SPIRE) observations at 70 , 160 , and $500 \mu\text{m}$ (Molinari et al. 2010a); two SOFIA/HAWC+ maps at 89 and $214 \mu\text{m}$ (Vaillancourt 2016); one ALMA map from the ALMA-IMF dataset at 1.3 mm , for which we used the free-free corrected cleanest dataset (see Sect. 4.2, Fig. 5d and Galván-Madrid et al. 2024). The associated flux uncertainties were 15% for LABOCA (Contreras et al. 2013), 20% for SABOCA (Lin et al. 2019), 10% and 7% for PACS and SPIRE (Galamez et al. 2014), 20% for HAWC+ (Chuss et al. 2019), and 10% for ALMA (G22) observations. All these details and numbers are provided in Sect. 2 of Dell’Ova et al. (2024). The associated synthetic PSF profiles range from $36''$ to $2.1''$. Dell’Ova et al. followed the procedure first introduced by Motte et al. (2018b) for a number of parameters. First, PPMAP products were generated with an expected angular resolution of $2.5''$. Second, in order to account for the different filtering of the data by these instruments, a high-pass filter was applied to the ground-based images during the PPMAP SED-fitting procedure. This is done by enabling the ‘high-pass’ PPMAP input parameter, which subtracts a constant background (the mean value across the image) from both the model and observed images for a set of specified wavelengths. This was applied to our ground-based observations to account for the suppressed low spatial frequencies. This parameter is listed in Table A.1. of the Dell’Ova et al. article. Finally, we first used eight modified black-body components between 21 and 39 K to fit the observations, and we then used the procedure they first applied to correct PPMAP dust temperatures for the effects of non-negligible optical depth of the dust at $70 \mu\text{m}$. We applied such a correction to our PPMAP outputs a posteriori, and it resulted in an increase of the maximum temperature in our field from 39 K to 44 K.

We then produced a map of column-density-averaged mean dust temperature, on which we performed a series of small-scale corrections. First, following Pouteau et al. (2022), we replaced

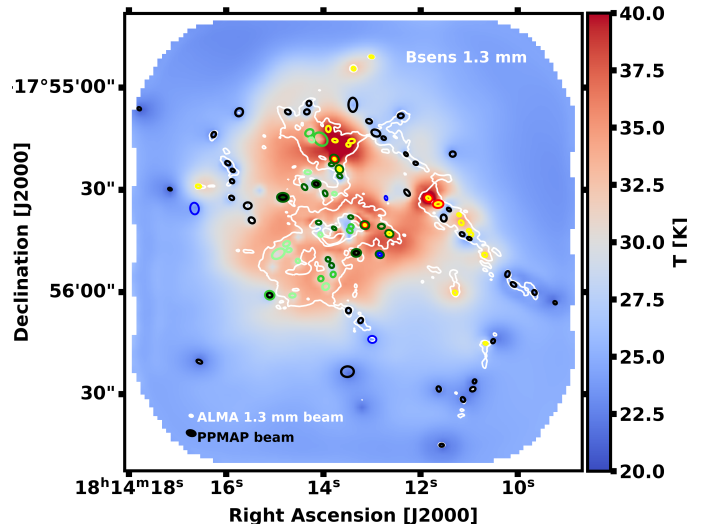


Fig. 10. PPMAP dust temperature map with an expected $2.5''$ resolution, overlaid with bsens 1.3 mm continuum emission (white contours) and cores from the *getsf* filtered core catalogue. The colours represent the different categories of cores that we identified as in Fig. 9. The average temperature in W33-Main is $27 \pm 3.5 \text{ K}$.

the temperature distribution within cores by 2D Gaussian with the following properties; the size was given by *getsf* and a maximum temperature given by the mean core temperature, increased by 4 K for protostellar cores to take into account internal heating, and decreased by 2 K for prestellar ones. For those, since we noted that the optical-thickness correction tended to result in high temperatures, we performed this subtraction on the values obtained without this correction. Finally, we noted that the two most massive hot core candidates (#1 and #2) appear as heating points in the PPMAP output. For them, we additionally estimated their mean temperature, taking into account extrapolating values measured in the expected $2.5''$ resolution element of the temperature map to the $\sim 1.5''$ size of the protostellar cores. With this methodology, we found temperatures of $55 \pm 10 \text{ K}$ for core #1 and $49 \pm 10 \text{ K}$ for core #2.

Figure 10 shows the dust temperature map at the expected $2.5''$ resolution, resulting from all these large- and small-scale corrections. The temperatures vary from 20 to 55 K. The average value of $27 \pm 3.5 \text{ K}$ is in agreement with that provided by M22 for evolved regions. On large scales, hot spots correspond to the three H II regions we identified, in which Beilis et al. (2022) posited the presence of OB-type stars: eight, eight, and two, respectively, in our regions 1, 2–3, and 4, although their conclusion is rather difficult to verify. The centre part of W33-Main is globally warm, and the outskirts of the region, where most of the prestellar cores are located, are colder. The Main-West filament has an average temperature of about 25 K.

Our values can be compared with temperatures inferred in various past studies. On the one hand, the prior cold-dust temperature map obtained with PPMAP by Marsh et al. (2017) in the W33-Main region is shown in Zhou et al. (2023) at $12''$ resolution. It was obtained applying PPMAP to data from the *Herschel* Hi-GAL programme (Molinari et al. 2010b, 2016). Their values, from 15 to 23.5 K are lower than ours. This could be explained by our $2.5''$ angular resolution for the output maps, as well as by their absence of optical thickness correction. I14 inferred a value of $42.5 \pm 12.6 \text{ K}$ for the cold dust, higher than our $27 \pm 3.5 \text{ K}$ average value. The apparently different values result from the

different methodologies: unlike I14, we performed the optical thickness (large-scale) corrections and a few small-scale corrections, and they constrained a $\beta = 1.2 \pm 0.4$ value different from our 1.8 one, and their measurement was obtained with a single-temperature fit of the mean spectral energy distribution over an aperture smaller than our field of view, not including interferometric data. In addition to this study, Tursun et al. (2022) performed an LTE analysis of molecular absorption in W33-Main. They used NH_3 lines with $E_{\text{low}} \geq 20$ K (within $\sim 4 \text{ pc}^2$) and inferred rotational temperatures of 23 and 38 K for the velocity components that they identified. They provided a kinetic temperature map, with values ranging from 15 to 45 K from the ratio of (2,2) to (1,1) lines, which seems compatible with our measurement.

6.2. The global core mass function in W33-Main

In order to estimate the masses of the cores in our catalogue, we used the formula in Motte et al. (2018b) and Pouteau et al. (2022) for our core sample:

$$M_{\tau \geq 1} = - \frac{\Omega_{\text{beam}} d^2 S_{1.3 \text{ mm}}^{\text{int}}}{\kappa_{1.3 \text{ mm}} S_{1.3 \text{ mm}}^{\text{peak}}} \ln \left(1 - \frac{S_{1.3 \text{ mm}}^{\text{peak}}}{\Omega_{\text{beam}} B_{1.3 \text{ mm}}(T_{\text{dust}})} \right). \quad (1)$$

This equation assumes that thermal dust emission at 1.3 mm is optically thick ($\tau_{1.3 \text{ mm}} \geq 1$), which we assume is the case at least in the densest cores. For W33-Main, we adopted a 2.4 kpc value for the distance d (see discussion in I14). In addition to this, $\kappa_{1.3 \text{ mm}}$ is the dust opacity per unit (gas + dust) mass at 1.3 mm, for which we adopted the value of $0.01^{+0.005}_{-0.0033} \text{ cm}^2 \text{ g}^{-1}$ from Ossenkopf & Henning (1994), with the same error bars as adopted by Pouteau et al. (2022) to account for its dependence with density and gas temperature. $B_{1.3 \text{ mm}}(T_{\text{dust}})$ is the Planck function computed using the dust temperature T_{dust} , and Ω_{beam} is the solid angle of the beam at 1.3 mm. T_{dust} is the individual core-averaged mean dust temperature produced from the temperature map described in the previous section after all small-scale corrections were applied (Fig. 10). Furthermore, this equation is based on both the peak flux density value of the dust continuum emission at 1.3 mm, $S_{1.3 \text{ mm}}^{\text{peak}}$ and the integrated flux density value of the dust continuum emission at 1.3 mm, $S_{1.3 \text{ mm}}^{\text{int}}$. Among the 80 cores identified in W33-Main, we identified 25 sources whose continuum emission at 1.3 mm was contaminated by free-free emission and their fluxes were corrected accordingly (see Sect. 4.2). Furthermore, we identified four line-contaminated cores and four hot-core candidates, whose flux densities are given by our *cleanest* dataset. For the 47 remaining sources, it is given by our *bsens* dataset. The uncertainty on the flux density values of the dust continuum emission at 1.3 mm is provided by the *getsf* procedure (see Sect. 4 for references).

We measured core masses from $0.03 M_{\odot}$ to $13.2 M_{\odot}$. The correction for the optical thickness at 1.3 mm is only applicable to the ten densest cores of our catalogue. This correction results in a 5–10% increase of the masses of these ten cores. The four hot-core candidates are the most optically thick ones, and the other optically thick ones are protostars or cores located inside the central H II region and contaminated by free-free emission. Only two cores have masses greater than $10 M_{\odot}$, the most massive cores are the four hot core candidates with a maximum mass of $13.2 M_{\odot}$ for core #1. We plot the complementary cumulative distribution form (hereafter cumulative form) of W33-Main's CMF thus obtained in Fig. 11.

We then fitted the high-mass end of the CMF above the completeness value ($1 M_{\odot}$, Sect. 4.1) by a power law of the

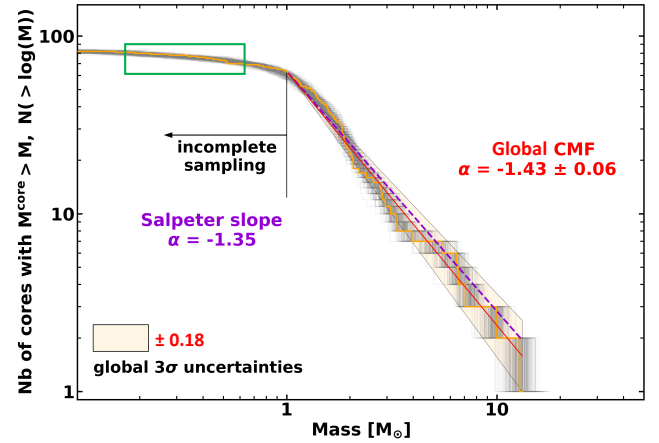


Fig. 11. Cumulative CMFs using temperature map (orange histogram and red curve). The mass-driven uncertainty is represented by grey histograms, and the global uncertainty is represented by a yellow-ish box (see Pouteau et al. 2022 for details). We represent the fit resulting from Salpeter value in a dashed purple line. The green box locates the seven free-free uncertain cores and the four CO-contaminated cores. The vertical black segment shows the completeness limit ($1.0 M_{\odot}$).

form $N(\geq \log M) \propto M^{\alpha}$. As Pouteau et al. (2022), we used the Alstott fitting method (Alstott et al. 2014, using a maximum likelihood estimate approach) and obtained a first estimate of $\alpha = -1.43 \pm 0.06$ ⁷. The uncertainty on this slope value is shown in Fig. 11. It is a quadratic sum of the uncertainty on the core mass (hereafter mass-driven uncertainty) and of that on the fitting procedure (hereafter fit uncertainty). The mass-driven uncertainty represents approximately $\sigma \approx 0.06$ on the final slope value. It was obtained by performing the fit over 2000 CMFs randomly generated from individual core masses (see Fig. 11) randomly comprised between M_{min} and M_{max} , the minimum and maximum mass values computed from the measured flux density, dust opacity at 1.3 mm, and dust temperature plus or minus the associated 1σ uncertainties (a map of mean dust temperature uncertainty was provided by PPMAP). The fit uncertainty was generally of the order of $\sigma \approx 0.02$ estimated from the associated χ^2 value.

Because the number of cores in our *getsf* catalogue is small, we then used a bootstrap procedure to better estimate the most probable slope value and its associated uncertainty. This procedure is fully described in Pouteau et al. (2023). 5000 core samples were generated from the observed core sample. In this bootstrapping part of the procedure, the masses are randomly drawn in a way that not all cores appear in every sample, and some cores appear in a sample multiple times. For each core, the mass is picked following a normal distribution. The center of this distribution is the core mass value, and its standard deviation value was equal to half the σ value associated with a core mass mentioned in the previous paragraph. Then each core distribution is fitted using the maximum likelihood estimate method of Alstott et al. (2014), and the fit values are gathered in a histogram. This fitting procedure also provides an estimate of the best lower mass limit for the fit, thus giving an additional uncertainty on the completeness level. All histograms are then fitted by an exponentially modified Gaussian (EMG), whose peak locates

⁷ For this global CMF, we verified that the $-2/+4$ K temperature corrections on prestellar and protostellar cores' temperatures induces only a minor change of the order of 10% for the individual masses and of 8% for the CMF's slope.

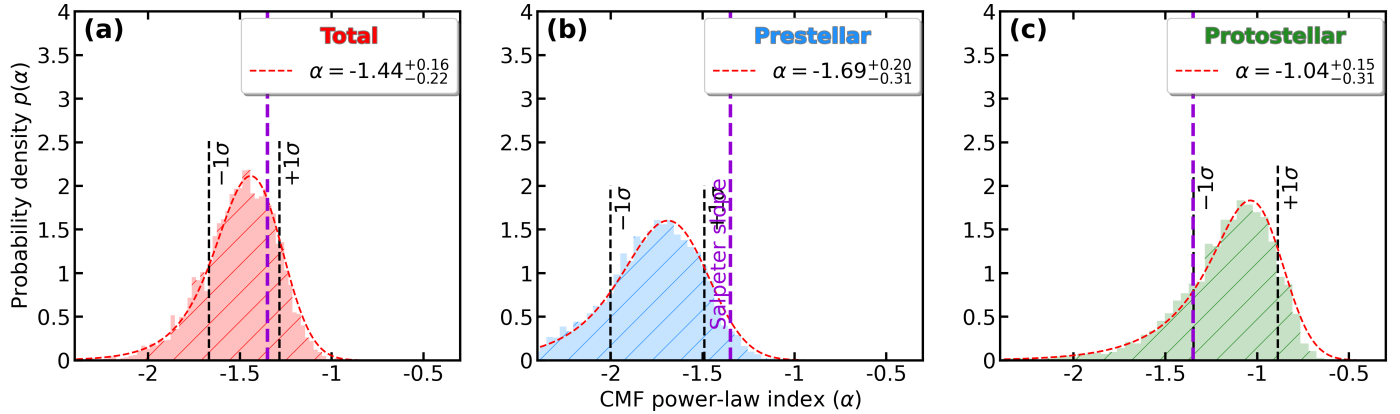


Fig. 12. Probability density as function of slope value of high-mass end of the CMF for (a) the global CMF in W33-Main, and (b) and (c) the prestellar and protostellar sub-populations of scenario A. The coloured histograms result from a bootstrap procedure including using the Alstott et al. (2014) method. The best slope value estimate, its uncertainty, and the starting point of the fit were determined by an exponentially modified Gaussian (EMG) (red dashed line). The 1σ errors (represented as vertical back-dashed lines) were determined by taking 68% of the slope values before and after the peak of the distribution. The Salpeter slope is represented by a purple-dashed line.

the best fit value for each core sample, with uncertainties determined to comprise the slope values in a $\pm 1\sigma$ range around the peak value. The resulting final slope value for the global CMF in W33-Main is $\alpha = -1.44^{+0.16}_{-0.22}$ (see Fig. 12). This global CMF power-law value is steeper, but consistent with the Salpeter one.

We note that if we do not apply flux correction for the 18 free-free-contaminated cores, we change the value from $\alpha = -1.44^{+0.16}_{-0.22}$ to $\alpha = -1.30^{+0.14}_{-0.19}$, which is consistent with the Salpeter slope. The change in the slope is significant as the flux correction decreases the masses of massive cores. If, in addition, we do not apply flux correction for the ten free-free-uncertain cores, we can observe an additional increase in intermediate-to-massive cores' numbers, changing the slope value to $\alpha = -1.22^{+0.13}_{-0.17}$ and moving away from the canonical IMF value of -1.35 . Without any flux correction for free-free contamination, we would have found a slightly top-heavy CMF. Finally, using a uniform dust temperature equal to the average of Fig. 10, $T_{\text{dust}} = 27$ K, the core masses range from $0.03 M_{\odot}$ to $28.2 M_{\odot}$. The resulting CMF has a slope value of $\alpha = -1.28^{+0.14}_{-0.22}$, which is i. slightly different from our non-uniform temperature value but compatible with it, and ii. slightly less than but compatible with the Salpeter value.

7. Discussion

7.1. Prestellar versus protostellar CMFs

In Sect. 5, we devised scenario A (59/21 prestellar and protostellar cores), and scenario B (43/37). In scenario A, the prestellar core masses range from $0.03 M_{\odot}$ to $7.4 M_{\odot}$, and the 21 protostellar core ones from $0.04 M_{\odot}$ to $13.2 M_{\odot}$. The most massive cores are the four hot-core candidates, hence protostellar cores. Only 3% of the prestellar cores have a mass greater than $5 M_{\odot}$ (this is the case for cores #4 and #5), against 19% of the protostellar cores. In scenario B, the prestellar core masses range from $0.05 M_{\odot}$ to $7.4 M_{\odot}$, and the 37 protostellar core ones from $0.03 M_{\odot}$ to $13.2 M_{\odot}$. The most massive cores are still the four hot-core candidates. 5% of the prestellar cores have a mass greater than $5 M_{\odot}$ (again, cores #4 and #5), against 11% of the protostellar cores.

Figure 13 shows the resulting cumulative CMFs for the two sub-populations in scenario A. We found first estimates

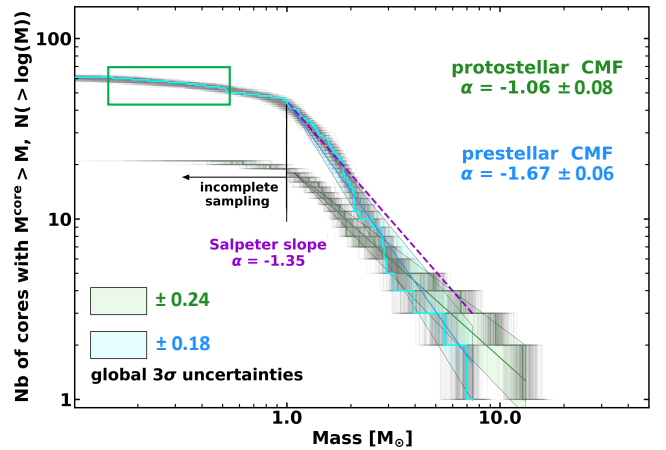


Fig. 13. Cumulative CMFs for prestellar (cyan histogram and blue curve) and protostellar (pale green histogram and green curve) cores in W33-Main (in scenario A). The light green and cyan boxes around the fits are the uncertainties on the mass values. We represent the fit resulting from Salpeter value with a dashed purple line. The green box locates the seven ‘free-free uncertain’ cores and the four CO-contaminated cores. The vertical black segment shows the completeness limit ($1.0 M_{\odot}$).

for slope values of $\alpha = -1.67 \pm 0.06$ for the prestellar cores, and $\alpha = -1.06 \pm 0.08$ for the protostellar ones⁸. We used the bootstrap procedure again, with resulting final slope values of $\alpha = -1.69^{+0.20}_{-0.31}$ for the prestellar cores and $\alpha = -1.04^{+0.15}_{-0.31}$ for the protostellar ones (see Fig. 12). The numbers we obtained for scenario B were not substantially different, with bootstrap values of $\alpha = -1.75^{+0.24}_{-0.42}$, $\alpha = -1.25^{+0.17}_{-0.33}$. All these results were obtained on relatively small samples and should be treated with caution.

Regardless of the scenario (A or B), we found that the prestellar CMF is steeper than the protostellar one in W33-Main and that the latter is slightly flatter (i.e. slightly top-heavy) but compatible with the Salpeter slope. In the W43-MM1, MM2,

⁸ We verified that these values were not significantly modified by the $-2/+4$ K temperature corrections on pre- and proto-stellar cores.

and MM3 sub-regions of the young W43 star-forming region, separating prestellar from protostellar cores with the same criteria as described in this study, Nony et al. (2023) also measured a steep slope value ($\alpha = -1.46_{-0.19}^{+0.12}$) for the prestellar CMF and a significantly flatter high-mass tail ($\alpha = -0.64_{-0.07}^{+0.05}$) than us for the protostellar one, compared with the Salpeter slope. The notable difference is that their prestellar core sub-sample's CMF was marginally compatible with the Salpeter slope. Combined with the lack of massive prestellar cores and deficit in low-mass protostellar cores⁹, the CMFs of W43-MM1, MM2, and MM3 were in agreement with the 'clump-fed' scenario (see e.g. Smith et al. 2009; Wang et al. 2010; Motte et al. 2018b; Vázquez-Semadeni et al. 2019). In this scenario, cores keep accreting matter during the protostellar phase, especially the massive ones that accrete matter more efficiently from the surrounding material. This results in an excess of massive protostellar cores, and in the absence of high-mass prestellar cores at the earliest stages of high-mass star formation (noted in infrared dark clouds; e.g. Sanhueza et al. 2017, 2019, and Morii et al. 2023). Overall, in W33-Main, we also found this excess of more massive protostellar cores and the absence of high-mass prestellar ones. We note that we found low-mass protostellar ones. In general, we defer the discussion on the low value of core masses throughout our observed field to the next section. In any case, the scenario where turbulent cores would individually collapse (see the discussion in, e.g. Motte et al. 2018a) is ruled out in W33-Main because i) we see a break in the slope of the CMF fit between the prestellar and protostellar phase, ii) our protostellar CMFs are only marginally compatible with Salpeter's fit, iii) we do not detect massive prestellar cores (although this could be because of their short lifetime), and iv) the prestellar cores we found are neither isolated nor pertaining to static environments. At later stages in the history of W33-Main, we cannot speculate about the fate of mass distributions, because our sub-samples are probably not statistically significant and also because the further mass conversion and fragmentation mechanisms might change our results in a highly uncertain way. Our attempts at applying the same prescriptions as Pouteau et al. (2022) to both our sub-samples yielded a too broad variety of outcomes to be conclusive.

7.2. A tentative global view on star formation in W33-Main

In this study, we show that W33-Main, which qualify as an evolved protocluster, displays a global CMF high-mass end with a slope close to Salpeter's (see Fig. 11). This is in stark contrast to the results obtained for the young and massive protoclusters W43-MM1 and W43-MM2 and the intermediate massive protocluster W43-MM3, where top-heavy global CMFs have been revealed (Motte et al. 2018b, Pouteau et al. 2022, 2023). These three clouds have approximately the same mass as W33-Main ($\sim 12 \times 10^3$, $\sim 17 \times 10^3$, $\sim 15 \times 10^3$, and $\sim 8 \times 10^3 M_{\odot}$ W33-Main, W43-MM1, MM2, and MM3, Dell'Ova et al. 2024) and have all been selected among the most massive protoclusters of the Milky Way. We therefore propose that the observed differences for the high-mass end slope of their CMFs are related to the difference in their evolutionary stage.

In young protoclusters, the main process that could influence the formation of cores and therefore the CMF is the formation of

the dense gas, in which cores and stars will form. In this framework, the core and star formation starts in the central part of the cloud, often called the hub. These structures present an atypical star formation activity due to their density and kinematics (see the review by Motte et al. 2018a and references therein). The global infall of the cloud, associated with hierarchical inflows of gas, would indeed preferentially feed massive cores while preventing lower mass cores from forming. Pouteau et al. (2022) proposed that a global top-heavy CMF would result from this very dynamic formation of clouds. They subdivided W43-MM2, and MM3 into six sub-regions and classified them into different evolutionary stages (from quiescent to burst and to post-burst) based on the surface density of cores, number of outflows, and UCH II presence. Looking at the CMF of each sub-region, they found that the high-mass tail of the CMF seemed to evolve from Salpeter-like to top-heavy when star formation enters a burst within the ridge or hub.

In evolved protoclusters, cloud formation could be nearly completed, while stellar feedback effects such as the development of H II regions are expected to have a significant impact on the cloud structure, temperature, and chemistry (see Galván-Madrid et al. 2024; Dell'Ova et al. 2024; Cunningham et al., in prep.). Subsequently, the surrounding infalling gas organises itself into dense filamentary structures that can host more slowly evolving (less massive) cores from the same generation as the protostars that drive the H II regions, or even a second generation of cores and eventually stars. Indeed, higher contrast N_2H^+ filaments are observed in evolved regions of ALMA-IMF (Stutz et al., in prep.; Cunningham et al., in prep.). This is the scenario that could be operating in W33-Main. The cloud is strongly impacted by the fastest evolving high-mass stars by means of three H II regions. The cloud gas is compressed at the periphery of the H II regions and it is heated; W33-Main has a median temperature 10 K higher than that of W43-MM1. In the case of W33-Main, the heating is also due to the proximity of nearby massive star clusters identified by Messineo et al. (2015).

Overall, we found 12 cores in the H II regions (representing 2.5% of the 1.3 mm map in surface, and containing approximately $700 M_{\odot}$), 12 cores in their surroundings (2%, $700 M_{\odot}$), and 56 cores in the rest of the cloud (95.5%, $10\,700 M_{\odot}$). Looking at the ratios of core number over either surface area or mass, we hence found that star formation is going on quite efficiently in the two first sub-regions. This is the first observational feature we need to interpret here. The second observational feature we aim to understand is the limitation of the maximum mass for cores detected with ALMA all over the observed field; in the H II regions the maximum core mass is about $7 M_{\odot}$, while it is $13 M_{\odot}$ in the surroundings and in the rest of the field. This is five to ten times less than in W43 (Nony et al. 2023). The discussion about the prestellar and protostellar distribution in the central regions is hampered by the confusion (scenario A leads to 18/6 and B leads to 3/21 prestellar and protostellar cores) and by the fact that this sub-sample of cores is not statistically significant. On the contrary, the region we defined as the rest of the cloud is unaffected by the choice between scenario A or B. It contains 56 cores, 15 of which are protostellar (which represents 27%; Nony et al. 2023 found 35% of the protostellar cores in the clouds of the W43 complex) and 41 are prestellar. In this region, there is no massive prestellar core; only two of those exceed $5 M_{\odot}$, for a maximum mass of $7.4 M_{\odot}$. We found a slight excess of massive protostellar cores (2/15 above $5 M_{\odot}$), but again with low maximum mass ($13.2 M_{\odot}$). In addition to this, we found low-mass protostellar cores (one at $0.4 M_{\odot}$, two around $1.4 M_{\odot}$). All these numbers suggest a growth in mass during the core evolution and

⁹ They found that the ratio of protostellar cores over prestellar cores is about 15% in the $0.8-3 M_{\odot}$ range, and this increases to reach 80% in the $16-110 M_{\odot}$ range. In addition, they found maximum masses of $109 M_{\odot}$ and $37 M_{\odot}$ for protostellar and prestellar cores, respectively.

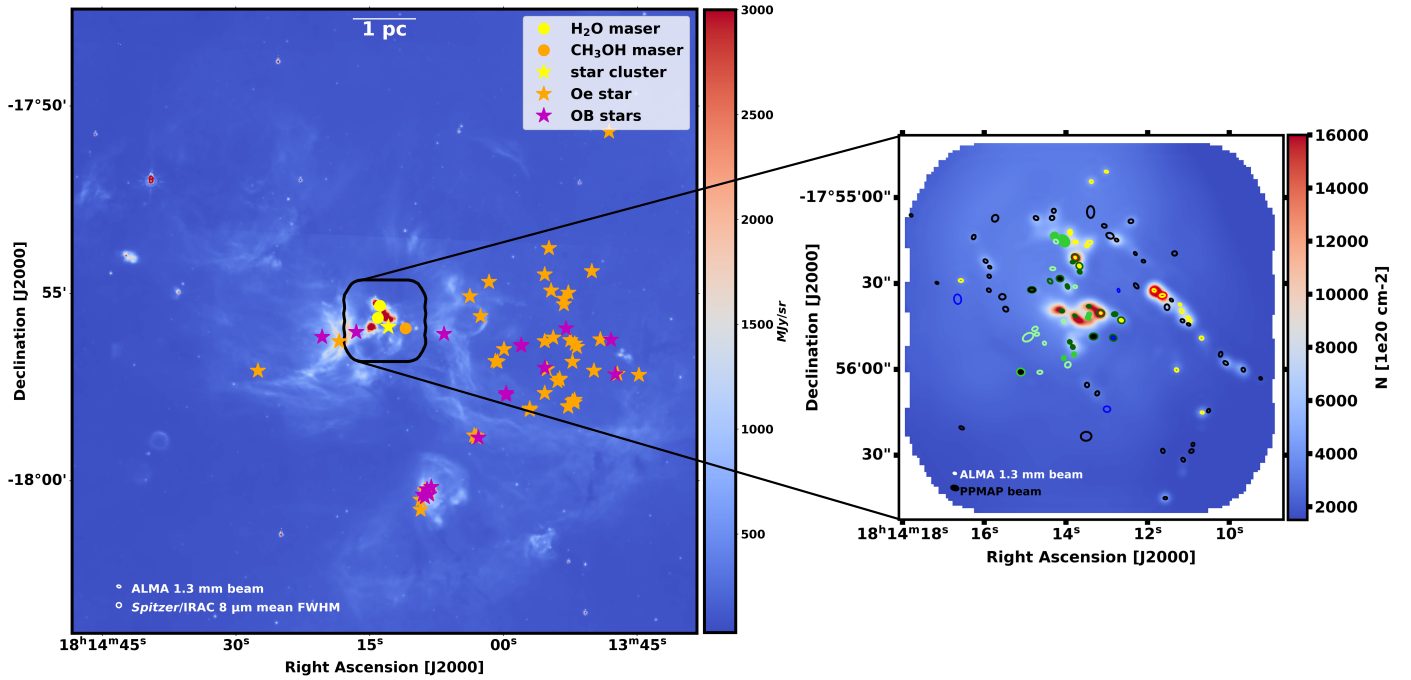


Fig. 14. Overview of W33 complex and stars within. *Left:* overview of W33 region seen in the 8 μm channel of the *Spitzer* telescope with a 2'' resolution. The coloured markers show the massive infrared sources identified using *Spitzer*/IRAC (Messineo et al. 2015). *Right:* PPMAP column density map with a 2.5'' resolution, with the cores from the *getsf* filtered core catalogue. The colours represent the different categories of cores identified in Figs. 9 and 10. The filled cores correspond to the ones located inside the H II regions and their surroundings (see definition in Sect. 3.5).

thus already confirm that the star formation in ‘the rest’ of the cloud occurs in a ‘clump-fed’ scenario.

We propose that the two observational features we want to interpret are due to stellar feedback conveyed by the formation of compression fronts and by the emission of energetic photons. On the one hand, the zoomed-in view of W33-Main in Fig. 14 shows the correlation of cores detected with ALMA with column density. It seems that the increased star formation efficiency in the central regions is favoured by the creation of compression fronts associated with the H II regions. We note that in the rest of the field, the core formation also seems to globally correlate with column density, in filaments probably caught in the global infall of the cloud. On the other hand, the limitation of the maximum core mass could be due to an effect of energetic photons emitted by the stars driving the H II regions for cores in the centre of our field, and by the clusters of massive stars detected by Messineo et al. (2015) and shown in Fig. 14 for the cores in the rest of the field observed by ALMA. The mechanism by which energetic photons limit the maximum mass of our cores could be by dispersing and/or ionising the less embedded parts of W33-Main, effectively cutting the feeding of clumps by low-mass cores. In this global picture, the ‘feedback’ is exerted from the outside of our field by already evolved, massive stars, and from the inside by the stars that drive the H II regions. Those could belong to the same generation as the cores that we detect. Indeed, the kinematical ages of the H II regions we observe is about few tens of thousands of years at maximum, with their sizes making them more evolved than ‘ultracompact H II regions’ (Hoare et al. 2007), and the typical lifetime of a precursor of an ultracompact H II region is no more than 10^5 years (Churchwell 2002). This lifetime argument and the fact that, for example, Messineo et al. (2015) did not detect any lower mass star in our field seems to indicate that the stars that drive the H II regions and the cores we detect belong to the same generation of star formation.

8. Conclusion

We presented the ALMA-IMF observations of the W33-Main star-forming region. Using ALMA lines and continuum observations, we provided an updated description of the region, a census of star-forming cores whose properties we measured, and built the local CMF. Our most significant findings are the following.

- In the 1.3 and 3 mm continuum datasets, we recovered the large-scale structures already highlighted in past studies, and we were able to uncover new structures thanks to the $\sim 1''$ angular resolution of the observations (see Sect. 3.3 and Fig. 2). Based on additional line emission maps in CO (2–1), SiO (5–4), and N_2H^+ ($v = 0, J = 1-0$), we discovered a network of numerous filaments as well as bipolar outflow structures, probably linked to star formation (in Sect. 3.4 and Fig. 3). We used the contours of H41 α (and to a lesser extent {He41 α +C41 α }) and Ne II (from Beilis et al. 2022) emission to define what we consider ‘H II regions’, ‘H II region surroundings’, and ‘the rest of the cloud’ (see Sect. 3.5 and Fig. 4). The presence of H II regions is a sign of the ‘evolved’ status of W33-Main.
- We used the *getsf* procedure on the 1.3 mm 12 m array image to extract 94 compact continuum sources. This constitutes our ‘filtered’ core catalogue, with a completeness level of 90% above $1 M_\odot$ (see Sect. 4.1). We found 35 cores in regions where the free-free emission was likely to contaminate or dominate the emission at 1.3 mm, and we classified them in ten free-free dominated-cores (which we removed from our further core catalogues), seven free-free-uncertain and 18 free-free-contaminated cores. For the last two categories (25 cores), we corrected the flux density for the contamination of the free-free emission (see Sect. 4.2, and Figs. 5 and 6). We also removed four cores from our catalogue because their emission at 1.3 mm was dominated

by lines; hence, they are most likely outflow knots (see Sect. 4.3). We also corrected the flux density for four additional cores whose emission at 1.3 mm was contaminated by line emission. At this stage, our core catalogue contained 80 sources.

- We constrained the evolutionary stage of these 80 sources in Sect. 5. Based on infrared data, we first found one clear association of our source #24 with a Class I source and one clear association of our source #19 with a methanol maser, and two less clear correlations between cores from our list and H₂O masers. We identified four hot-core candidates using complex organic molecule spectra (Fig. 7) and 20 cores associated with either CO and/or SiO outflows (see Fig. 8 for examples). All four hot-core candidates are associated with outflows, but the Class I source is not, and hence we counted 21 robust protostellar sources. In scenario A, we consider them to be only protostellar (and the 59 others to be prestellar). For 16 cores, though, their location in free-free-contaminated regions made the association with an outflow unclear. In scenario B, we included them in the protostellar sub-sample (for a tally of 37 protostellar and 43 prestellar cores). Our findings on the nature of cores can be found in Fig. 9.
- We then converted the flux densities at 1.3 mm for all of our cores to masses. This conversion depends on dust temperature, which we obtained using the PPMAP procedure (see Fig. 10) and core-scale prescriptions. The resulting CMF built from the complete core sample of W33-Main has a power-law behaviour with a slope slightly steeper than, but consistent with, the Salpeter value ($\alpha = -1.44^{+0.16}_{-0.22}$; see Figs. 11 and 12 in Sect. 6). Once split in prestellar and protostellar sub-samples (see Sect. 7), we found respective values of $\alpha = -1.69^{+0.20}_{-0.31}$ and $\alpha = -1.04^{+0.15}_{-0.31}$ (scenario A; see Fig. 13) and $\alpha = -1.75^{+0.24}_{-0.42}$ and $\alpha = -1.25^{+0.17}_{-0.33}$ (scenario B).
- These results were obtained on small samples and should be treated with caution. However, they are compatible with a ‘clump-fed’ scenario of star formation in an evolved cloud having already gone through hierarchical infall and where stellar feedback is operating in the form of H II regions probably driven by the most massive stars belonging to the same generation as the cores we detected, and also through energetic photons emitted by massive stars located outside of W33-Main. The masses of protostellar cores are a bit higher than those of the prestellar ones, the proportion of massive protostars is higher than that of the prestellar ones, there are no massive prestellar cores, but some low-mass protostellar ones. The star formation seems to proceed more efficiently in the central region, which could be due to the compression fronts generated by the H II regions. The cores’ masses are low in the whole observed field, which could be due to energetic photons emitted by the stars driving the H II regions and by massive stars outside W33-Main.

Our results call for investigations in a statistical sample of evolved regions. Indeed, our results differ from those found in less evolved, young, star-forming regions by the ALMA-IMF programme. If confirmed, the CMF of massive protoclusters could initially be top-heavy, but steepen to reconcile with the Salpeter IMF due to i) feedback effects exerted by stars (either from previous generations or the fastest evolving ones from the same generation) on the cloud, and/or ii) dynamical relaxation of the region leading to the formation of less dense filaments harbouring the new cores, and/or iii) the transformation of the most massive cores of the same generation in massive stars having already occurred. Our results perhaps also call for dedicated

investigations on peculiar sources found in our sample such as ‘uncertain’ sources, which are contaminated cores associated with outflows or located at the centre of the most prominent H II region.

Acknowledgements. We are grateful to the anonymous referee for the various suggestions that resulted in a significant improvement of this article. This article makes use of the ALMA data ADS/JAO.ALMA#2017.1.01355.L. ALMA is a partnership of ESO (representing its member states), NSF (USA) and NINS (Japan), together with NRC (Canada), MOST and ASIAA (Taiwan), and KASI (Republic of Korea), in cooperation with the Republic of Chile. The Joint ALMA Observatory is operated by ESO, AUI/NRAO and NAOJ. The project leading to this publication has received support from ORP, that is funded by the European Union’s Horizon 2020 research and innovation programme under grant agreement No 101004719 [ORP]. F.M., N.C., and F.L. also acknowledge support from the European Research Council (ERC) via the ERC Synergy Grant ECOGAL (grant 855130), from the French Agence Nationale de la Recherche (ANR) through the project COSMHIC (ANR-20-CE31-0009), and the French Programme National de Physique Stellaire and Physique et Chimie du Milieu Interstellaire (PNPS and PCMI) of CNRS/INSU (with INC/INP/IN2P3). R.G.M. and D.D.G. acknowledge support from UNAM-PAPIIT project IN108822, and from CONACyT Ciencia de Frontera project ID: 86372. This publication makes use of data products from the Two Micron All Sky Survey, which is a joint project of the University of Massachusetts and the Infrared Processing and Analysis Center/California Institute of Technology, funded by the National Aeronautics and Space Administration and the National Science Foundation. This publication makes use of data products from the Wide-field Infrared Survey Explorer, which is a joint project of the University of California, Los Angeles, and the Jet Propulsion Laboratory/California Institute of Technology, funded by the National Aeronautics and Space Administration. This publication also uses data from the ATLASGAL project, a collaboration between the Max-Planck-Gesellschaft, the European Southern Observatory (ESO) and the Universidad de Chile. It includes projects E-181.C-0885, E-078.F-9040(A), M-079.C-9501(A), M-081.C-9501(A) plus Chilean data. This work is based in part on observations made with the *Spitzer* Space Telescope, which was operated by the Jet Propulsion Laboratory, California Institute of Technology under a contract with NASA. PS was partially supported by a Grant-in-Aid for Scientific Research (KAKENHI Number JP22H01271 and JP23H01221) of JSPS. Melisse Bonfand is a postdoctoral fellow in the University of Virginia’s VICO collaboration and is funded by grants from the NASA Astrophysics Theory Program (grant number 80NSSC18K0558) and the NSF Astronomy & Astrophysics program (grant number 2206516). A.G. acknowledges support from the NSF via grants AST 2008101 and CAREER 2142300. A.S. gratefully acknowledges support by the Fondecyt Regular (project code 1220610), and ANID BASAL projects ACE210002 and FB210003.

References

- Aguirre, J. E., Ginsburg, A. G., Dunham, M. K., et al. 2011, *ApJS*, **192**, 4
- Allen, L. E., Calvet, N., D’Alessio, P., et al. 2004, *ApJS*, **154**, 363
- Alstott, J., Bullmore, E., & Plenz, D. 2014, *PLoS ONE*, **9**, e85777
- André, P., Di Francesco, J., Ward-Thompson, D., et al. 2014, in *Protostars and Planets VI*, eds. H. Beuther, R. S. Klessen, C. P. Dullemond, & T. Henning, 27
- Bastian, N., Covey, K. R., & Meyer, M. R. 2010, *ARA&A*, **48**, 339
- Beilis, D., Beck, S., & Lacy, J. 2022, *MNRAS*, **509**, 2234
- Bonfand, M., Csengeri, T., Bontemps, S., et al. 2024, *A&A*, in press, <https://doi.org/10.1051/0004-6361/202347856>
- Brouillet, N., Despois, D., Molet, J., et al. 2022, *A&A*, **665**, A140
- Carlhoff, P., Nguyen Luong, Q., Schilke, P., et al. 2013, *A&A*, **560**, A24
- Churchwell, E. 2002, *ARA&A*, **40**, 27
- Churchwell, E., Babler, B. L., Meade, M. R., et al. 2009, *PASP*, **121**, 213
- Chuss, D. T., Andersson, B. G., Bally, J., et al. 2019, *ApJ*, **872**, 187
- Contreras, Y., Schuller, F., Urquhart, J. S., et al. 2013, *A&A*, **549**, A45
- Csengeri, T., Urquhart, J. S., Schuller, F., et al. 2014, *A&A*, **565**, A75
- Csengeri, T., Bontemps, S., Wyrowski, F., et al. 2017, *A&A*, **601**, A60
- Cunningham, N., Ginsburg, A., Galván-Madrid, R., et al. 2023, *A&A*, **678**, A194
- Dell’Ova, P., Motte, F., Gusdorf, A., et al. 2024, *A&A*, in press, <https://doi.org/10.1051/0004-6361/202348984>
- Dewangan, L. K., Baug, T., & Ojha, D. K. 2020, *MNRAS*, **496**, 1278
- Díaz-González, D. J., Galván-Madrid, R., Ginsburg, A., et al. 2023, *ApJS*, **269**, 55
- Edwin Salpeter, E. E. 1955, *ApJ*, **121**, 161
- Enoch, M. L., Evans, Neal J., I., Sargent, A. I., et al. 2008, *ApJ*, **684**, 1240
- Frank, A., Ray, T. P., Cabrit, S., et al. 2014, in *Protostars and Planets VI*, eds. H. Beuther, R. S. Klessen, C. P. Dullemond, & T. Henning, 451
- Galametz, M., Albrecht, M., Kennicutt, R., et al. 2014, *MNRAS*, **439**, 2542

- Galván-Madrid, R., Díaz-González, D. J., Motte, F., & Ginsburg, A. 2024, *ApJS*, submitted
- Ginsburg, A., Glenn, J., Rosolowsky, E., et al. 2013, *ApJS*, 208, 14
- Ginsburg, A., Anderson, L. D., Dicker, S., et al. 2020, *ApJS*, 248, 24
- Ginsburg, A., Csengeri, T., Galván-Madrid, R., et al. 2022, *A&A*, 662, A9
- Herbst, E., & van Dishoeck, E. F. 2009, *ARA&A*, 47, 427
- Hoare, M. G., Kurtz, S. E., Lizano, S., Keto, E., & Hofner, P. 2007, in *Protostars and Planets V*, eds. B. Reipurth, D. Jewitt, & K. Keil, 181
- Hosek, M. W. Jr., Lu, J. R., Anderson, J., et al. 2019, *ApJ*, 870, 44
- Immer, K., Reid, M. J., Menten, K. M., Brunthaler, A., & Dame, T. M. 2013, *A&A*, 553, A117
- Immer, K., Galván-Madrid, R., König, C., Liu, H. B., & Menten, K. M. 2014, *A&A*, 572, A63
- Khan, S., Pandian, J. D., Lal, D. V., et al. 2022, *A&A*, 664, A140
- Koenig, X. P., & Leisawitz, D. T. 2014, *ApJ*, 791, 131
- Kohno, M., Torii, K., Tachihara, K., et al. 2018, *PASJ*, 70, S50
- Kong, S. 2019, *ApJ*, 873, 31
- Könyves, V., André, P., Men'shchikov, A., et al. 2015, *A&A*, 584, A91
- Könyves, V., André, P., Arzoumanian, D., et al. 2020, *A&A*, 635, A34
- Kroupa, P., Weidner, C., Pflamm-Altenburg, J., et al. 2013, in *Planets, Stars and Stellar Systems*, 5: Galactic Structure and Stellar Populations, eds. T. D. Oswalt, & G. Gilmore, 115
- Lin, Y., Csengeri, T., Wyrowski, F., et al. 2019, *A&A*, 631, A72
- Liu, X.-L., Xu, J.-L., Wang, J.-J., et al. 2021, *A&A*, 646, A137
- Louvet, F., Motte, F., Hennebelle, P., et al. 2014, *A&A*, 570, A15
- Louvet, F., Motte, F., Gusdorf, A., et al. 2016, *A&A*, 595, A122
- Louvet, F., Motte, F., Ginsburg, A., et al. 2023, *A&A*, submitted
- Lu, J. R., Do, T., Ghez, A. M., et al. 2013, *ApJ*, 764, 155
- Maia, F. F. S., Moraux, E., & Joncour, I. 2016, *MNRAS*, 458, 3027
- Marsh, K. A., Whitworth, A. P., & Lomax, O. 2015, *MNRAS*, 454, 4282
- Marsh, K. A., Whitworth, A. P., Lomax, O., et al. 2017, *MNRAS*, 471, 2730
- Men'shchikov, A. 2021a, *A&A*, 654, A78
- Men'shchikov, A. 2021b, *A&A*, 649, A89
- Messineo, M., Clark, J. S., Figer, D. F., et al. 2015, *ApJ*, 805, 110
- Molinari, S., Swinyard, B., Bally, J., et al. 2010a, *A&A*, 518, A100
- Molinari, S., Swinyard, B., Bally, J., et al. 2010b, *PASP*, 122, 314
- Molinari, S., Schisano, E., Elia, D., et al. 2016, *A&A*, 591, A149
- Morii, K., Sanhueza, P., Nakamura, F., et al. 2023, *ApJ*, 950, 148
- Motte, F., André, P., & Neri, R. 1998, *A&A*, 336, 150
- Motte, F., André, P., Ward-Thompson, D., & Bontemps, S. 2001, *A&A*, 372, L41
- Motte, F., Bontemps, S., & Louvet, F. 2018a, *ARA&A*, 56, 41
- Motte, F., Nony, T., Louvet, F., et al. 2018b, *Nat. Astron.*, 2, 478
- Motte, F., Bontemps, S., Csengeri, T., et al. 2022, *A&A*, 662, A8
- Murase, T., Handa, T., Hirata, Y., et al. 2022, *MNRAS*, 510, 1106
- Nguyen Luong, Q., Motte, F., Schuller, F., et al. 2011, *A&A*, 529, A41
- Nguyen Luong, Q., Motte, F., Carlhoff, P., et al. 2013, *ApJ*, 775, 88
- Nony, T., Galván-Madrid, R., Motte, F., et al. 2023, *A&A*, 674, A75
- Ossenkopf, V., & Henning, T. 1994, *A&A*, 291, 943
- Pety, J., Guzmán, V. V., Orkisz, J. H., et al. 2017, *A&A*, 599, A98
- Planck Collaboration XXIV. 2011, *A&A*, 536, A24
- Planck Collaboration XII. 2014, *A&A*, 571, A12
- Planck Collaboration Int. XVII. 2014, *A&A*, 566, A55
- Pouteau, Y., Motte, F., Nony, T., et al. 2022, *A&A*, 664, A26
- Pouteau, Y., Motte, F., Nony, T., et al. 2023, *A&A*, 674, A76
- Sanhueza, P., Jackson, J. M., Zhang, Q., et al. 2017, *ApJ*, 841, 97
- Sanhueza, P., Contreras, Y., Wu, B., et al. 2019, *ApJ*, 886, 102
- Schneider, F. R. N., Sana, H., Evans, C. J., et al. 2018, *Science*, 359, 69
- Schuller, F., Menten, K. M., Contreras, Y., et al. 2009, *A&A*, 504, 415
- Skrutskie, M. F., Cutri, R. M., Stiening, R., et al. 2006, *AJ*, 131, 1163
- Smith, R. J. 2014, *MNRAS*, 443, L69
- Smith, R. J., Longmore, S., & Bonnell, I. 2009, *MNRAS*, 400, 1775
- Snell, R. L., Loren, R. B., & Plambeck, R. L. 1980, *ApJ*, 239, L17
- Takemura, H., Nakamura, F., Kong, S., et al. 2021, *ApJ*, 910, L6
- Testi, L., & Sargent, A. I. 1998, *ApJ*, 508, L91
- Towner, A. P. M., Ginsburg, A., Dell'Ova, P., et al. 2024, *ApJ*, 960, 48
- Tursun, K., Henkel, C., Esimbek, J., et al. 2022, *A&A*, 658, A34
- Vaillancourt, J. 2016, *Characterizing the FIR polarization spectrum in Galactic Clouds*, SOFIA Proposal, Cycle 5, ID. 05_0038
- Vázquez-Semadeni, E., Palau, A., Ballesteros-Paredes, J., Gómez, G. C., & Zamora-Avilés, M. 2019, *MNRAS*, 490, 3061
- Wang, P., Li, Z.-Y., Abel, T., & Nakamura, F. 2010, *ApJ*, 709, 27
- Westerhout, G. 1958, *Bull. Astron. Inst. Netherlands*, 14, 215
- Wright, E. L., Eisenhardt, P. R. M., Mainzer, A. K., et al. 2010, *AJ*, 140, 1868
- Xu, J.-L., Wang, J.-J., & Miller, M. 2011, *ApJ*, 727, 81
- Zhang, B., Moscadelli, L., Sato, M., et al. 2014, *ApJ*, 781, 89
- Zhang, Z.-Y., Romano, D., Ivison, R. J., Papadopoulos, P. P., & Matteucci, F. 2018, *Nature*, 558, 260
- Zhou, J.-W., Li, S., Liu, H.-L., et al. 2023, *MNRAS*, 519, 2391

Appendix A: Search for class I, II, and masers

Using archival observations in the mid-infrared and mid-near-infrared ranges, we attempted to identify if low-mass objects at advanced stages of evolution (class I, II and older) are present in this region, and if so, to assess their evolutionary stage based on their infrared fluxes.

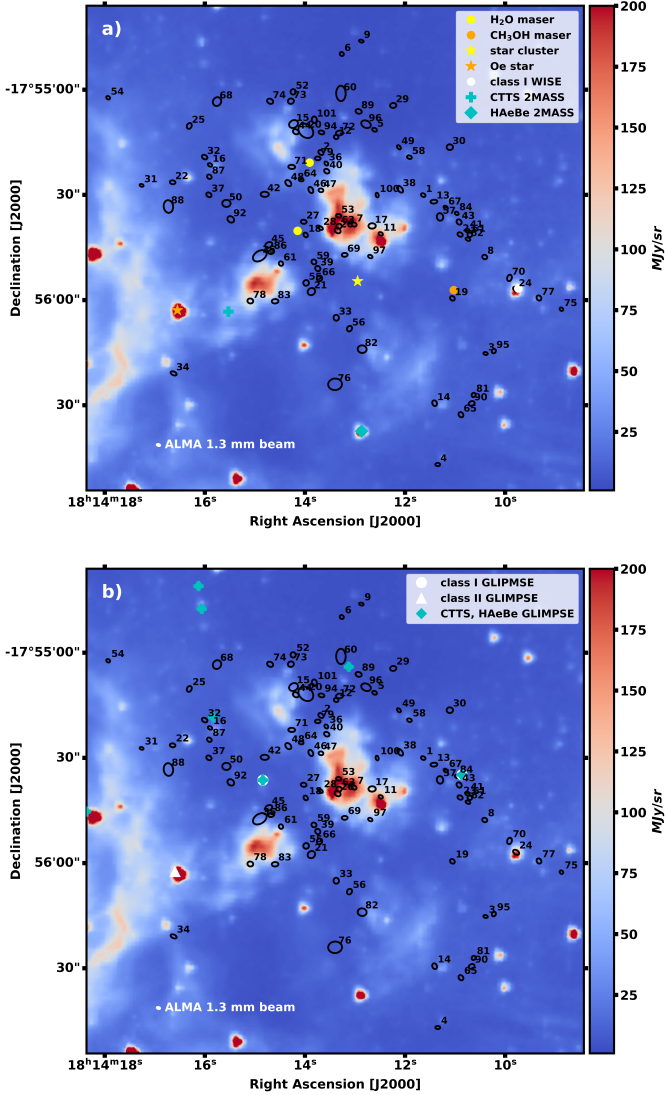


Fig. A.1. IRAC 3.6 μm map of W33-Main field observed by ALMA-IMF, reprojected on the ALMA 1.3 mm bsens dataset, with the cores from the *getsf* filtered catalogue in black ellipses. *Panel a*: In coloured markers are the infrared sources identified using 2MASS (cyan), WISE (white), and *Spitzer*/IRAC (Messineo et al. 2015) (other colors). *Panel b*: In coloured markers are the infrared sources identified using GLIMPSE.

A.1. 2MASS and WISE all-sky surveys

The W33 complex was fully mapped by both the 2MASS (Skrutskie et al. 2006) and WISE (Wright et al. 2010) all-sky surveys. 2MASS operates between 1.235 μm and 2.159 μm , and WISE between 3.4 μm and 22 μm . A total of 117 point sources in the 2MASS All-Sky Point Source Catalogue and 19 point sources in the AllWISE Source Catalogue were found in the W33-Main field observed by the ALMA-IMF Large

Programme. In order to reject false positives, we applied several selection criteria to these primary point source catalogues. Our method required simultaneous detections in the W_1 , W_2 bands of WISE or in the J, H, and K bands of 2MASS, and we then only selected the sources with a signal-to-noise ratio greater than two in these bands. After this selection, 32 point sources remained for the 2MASS catalogue and ten remained for the WISE one.

We then applied colour-colour criteria to these remaining point sources to select young stellar object candidates. For 2MASS objects, we compared the relative flux in the J, H, and K bands. We used the empirical colour criteria introduced by Xu et al. (2011). This set of conditions between the fluxes in various channels allowed us to distinguish cool giants, normally reddened stars, Classical T Tauri stars, He Ae/Be stars, and in general, infrared excess sources, including young stellar objects that do not fall into any of these categories. Similarly, we used a colour-colour criterion (Koenig & Leisawitz 2014) to characterise the point sources from the flux measurements of bands W_1 , W_2 , and W_3 of WISE. With these, we distinguished two evolutionary stages: Class I and Class II protostars, defined by their respective infrared excess. After the colour-colour filtering of the catalogues, the total amount of remaining point sources is three (one CTTS and two HAeBe) for 2MASS and one Class I for WISE within the field observed by the ALMA-IMF programme. We also included the point sources catalogued by Messineo et al. (2015) in this study: one star cluster, one O-type star, two water masers, and one methanol maser.

Our results can be seen in Fig. A.1a. We found a clear association between our prestellar core #24 and a Class I protostar detected in the WISE catalogue. For this core, we retained the protostellar classification. We also found a possible association between our protostellar core #19 and a CH_3OH maser, and two other potential associations between several of our sources with the two water masers. We note, however, that for these water masers, the association is more ambiguous than for the methanol maser: one is located within the H II region ‘2-3’ near cores #27 and #18, and the other one in a H II region surroundings between region ‘2-3’ and region ‘4’, near cores #71 and #79.

A.2. GLIMPSE Galactic plane survey

The W33 complex was also fully mapped by the GLIMPSE (Churchwell et al. 2009) Galactic plane survey. GLIMPSE I imaged at wavelengths 3.6, 4.5, 5.8, and 8.0 μm using the IRAC instrument (Infrared Array Camera) of the *Spitzer* telescope. A total of 210 point sources in the GLIMPSE I Catalogue were found in the W33-Main field observed by the ALMA-IMF Large programme. In order to reject false positives, we applied several selection criteria to this primary catalogue of point sources: our method required simultaneous detections in all IRAC bands, and we then only selected the sources with a signal-to-noise ratio greater than two in these bands. After this selection, 46 point sources remained in the GLIMPSE catalogue.

We then applied colour-colour criteria to these remaining point sources to select young stellar object candidates. We compared the relative flux in all the four bands. We used the colour-colour criteria of Allen et al. (2004). This set of conditions between bands [3.6]-[4.5] and [5.8]-[8.0] allowed us to distinguish between three evolutionary stages: Class I, Class II, and more evolved protostars (CTTS and HAeBe), defined

by their respective infrared excess. After this colour-colour filtering of the catalogue, six Class I, one Class II, and seven more evolved objects were found within the field observed by the ALMA-IMF program.

These results can be seen in Fig. A.1b. We found one Class I protostar not associated with any of our cores, and one source that could be classified either as a Class I or a Class II protostar, not associated with any of our cores, but whose position correlates with the Oe star classified by [Messineo et al. \(2015\)](#)¹⁰. We found four CTTS or HAeBe stars with no association with any of our cores, and three of them with a potential but unclear association with our cores: two between prestellar cores (one between #60 and #89 and one between #32 and #16), and one between the two protostellar cores #84 and #43. We did not find any association between point sources identified using the 2MASS and WISE catalogues on the one hand, and the GLIMPSE catalogue on the other hand.

Appendix B: Complementary figure and table

We estimated a 90% global completeness level of $1.0 \pm 0.2 M_{\odot}$ for the *getsf* catalogue based on the method presented in Sect. 4.1. Fig. B.1 details how it was reached in W33-Main.

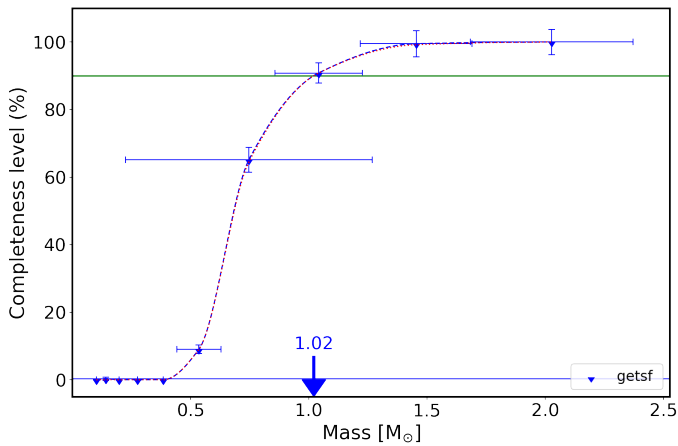


Fig. B.1. Completeness level of ~ 800 synthetic cores added on background image of W33-Main. The core content is 90% complete down to $1.0 \pm 0.2 M_{\odot}$ for the *getsf* catalogue. The error bars represent the $\pm 1\sigma$ uncertainties for mass estimates across each bin (*x-axis*) and total cores retrieved per bin (*y-axis*). Data points were interpolated using the piecewise cubic hermite interpolating polynomial method. Blue points represent the full sample of cores detected by *getsf*

¹⁰ The fact that this source can simultaneously be classified a Class I or II protostar or as a Oe star illustrates the uncertainty of this kind of search.

Table B.1. Table of properties of 94 sources extracted by *getsf* in W33-Main using the 1.3 mm bsens continuum map ('filtered' catalogue).

n	R.A. [J2000] h m s	Dec. [J2000] ° ' "	$a_{1.3 \text{ mm}}$ $b_{1.3 \text{ mm}}$ [pix × pix]	PA _{1.3 mm} [deg]	$S_{1.3 \text{ mm}}^{\text{peak}}$ [mJy beam ⁻¹]	$S_{1.3 \text{ mm}}^{\text{int}}$ [mJy]	$a_{3 \text{ mm}}$ $b_{3 \text{ mm}}$ [pix × pix]	×	PA _{3 mm} [deg]	$S_{3 \text{ mm}}^{\text{peak}}$ [mJy beam ⁻¹]	$S_{3 \text{ mm}}^{\text{int}}$ [mJy]	Gext2D (^(a)) tag	Nature (^(b))
1	18:14:11.84	-17:55:32.45	7.5 × 5.5	64	195.20 ± 10.51	306.80 ± 10.20	10.3 × 8.6	—	60	24.32 ± 1.24	28.77 ± 0.96	**	Hot core
2	18:14:13.77	-17:55:20.99	9.1 × 6.6	46	112.30 ± 4.02	272.20 ± 5.96	9.4 × 8.2	—	11	11.41 ± 4.50	10.63 ± 3.47	**	Free-free, hot core
3	18:14:10.66	-17:56:15.12	7.0 × 4.6	77	35.81 ± 1.01	45.70 ± 1.05	9.2 × 7.9	—	74	3.64 ± 0.23	3.87 ± 0.20	**	Outflows
4	18:14:11.56	-17:56:45.02	7.6 × 5.1	89	46.08 ± 1.37	65.64 ± 1.33	10.0 × 7.8	—	79	7.15 ± 0.31	8.03 ± 0.25	**	Outflows
5	18:14:12.76	-17:55:14.86	7.9 × 5.7	64	36.54 ± 1.31	69.93 ± 1.64	14.0 × 13.1	—	110	4.66 ± 1.55	9.31 ± 1.35	**	Outflows
6	18:14:13.38	-17:54:54.46	6.8 × 5.9	52	19.32 ± 1.02	29.58 ± 1.06	10.3 × 8.2	—	42	3.42 ± 0.35	4.26 ± 0.32	**	Free-free, hot core
7	18:14:13.14	-17:55:40.39	8.2 × 6.4	70	93.65 ± 16.36	178.50 ± 16.87	10.3 × 10.0	—	2	16.26 ± 14.10	22.94 ± 10.87	**	Outflows
8	18:14:10.68	-17:55:49.13	8.2 × 6.9	68	19.37 ± 1.29	40.63 ± 1.51	10.8 × 10.3	—	48	2.38 ± 0.46	3.24 ± 0.35	**	Outflows
9	18:14:13.01	-17:54:50.98	7.4 × 4.4	76	18.35 ± 0.76	21.25 ± 0.66	9.5 × 7.4	—	87	2.38 ± 0.26	2.96 ± 0.24	**	Free-free, outflows
11	18:14:12.64	-17:55:42.90	7.2 × 5.1	67	21.41 ± 1.27	29.40 ± 1.14	—	—	—	≤ 1.631	≤ 1.631	**	Outflows
12	18:14:13.48	-17:55:16.81	7.3 × 6.5	68	24.29 ± 2.25	41.37 ± 2.19	—	—	—	≤ 0.723	≤ 0.723	**	Hot core
13	18:14:11.64	-17:55:34.22	10.9 × 6.1	93	63.11 ± 10.08	116.70 ± 10.21	12.6 × 9.3	—	91	9.12 ± 1.18	12.20 ± 0.95	**	Free-free, outflow ?
14	18:14:11.62	-17:56:28.51	9.3 × 7.2	22	7.27 ± 0.42	19.87 ± 0.58	15.3 × 14.6	—	86	0.94 ± 0.19	2.94 ± 0.22	**	Free-free, outflow ?
15	18:14:14.29	-17:55:13.31	14.7 × 11.8	120	22.59 ± 6.05	112.80 ± 7.74	14.8 × 11.3	—	120	53.37 ± 17.81	108.60 ± 15.19	**	Free-free, outflow ?
16	18:14:15.86	-17:55:24.33	7.3 × 5.1	61	15.07 ± 1.25	20.55 ± 1.04	10.9 × 8.5	—	87	2.86 ± 0.41	4.16 ± 0.41	**	Free-free, outflow ?
17	18:14:12.80	-17:55:40.76	11.6 × 8.6	92	7.75 ± 3.60	22.37 ± 3.90	13.6 × 10.0	—	39	71.26 ± 32.10	105.50 ± 24.77	**	Free-free
18	18:14:14.06	-17:55:43.19	8.1 × 6.2	38	25.02 ± 11.94	39.59 ± 9.22	13.9 × 13.1	—	20	0.99 ± 0.30	2.26 ± 0.30	**	CH ₃ OH maser
19	18:14:11.29	-17:56:00.26	8.1 × 6.7	46	8.36 ± 0.86	17.54 ± 0.94	17.3 × 12.9	—	17	30.22 ± 14.69	77.31 ± 15.81	**	Free-free, outflow ?
20	18:14:14.05	-17:55:15.15	26.0 × 20.0	49	10.24 ± 3.71	139.70 ± 8.10	17.3 × 14.1	—	124	25.97 ± 8.43	81.02 ± 8.76	**	Outflows
21	18:14:13.95	-17:55:58.44	12.3 × 10.9	127	13.27 ± 2.48	71.46 ± 4.04	16.0 × 14.3	—	138	1.66 ± 0.33	4.29 ± 0.33	**	CO-contaminated
22	18:14:16.57	-17:55:29.00	8.8 × 6.2	83	9.77 ± 0.85	20.98 ± 0.99	11.1 × 9.3	—	0	3.42 ± 0.57	5.30 ± 0.57	**	Class I
23	18:14:11.14	-17:55:43.07	8.6 × 6.5	62	20.09 ± 4.38	38.03 ± 4.25	12.3 × 8.8	—	55	3.32 ± 0.52	4.51 ± 0.41	**	Free-free, outflow ?
24	18:14:10.09	-17:55:57.82	10.6 × 6.6	57	17.04 ± 2.18	40.28 ± 2.20	13.8 × 11.2	—	0	0.50 ± 0.34	0.59 ± 0.35	**	Free-free, outflow ?
25	18:14:16.25	-17:55:13.82	9.7 × 7.3	153	6.86 ± 0.81	21.06 ± 1.08	13.7 × 12.1	—	68	59.68 ± 43.04	116.40 ± 33.17	**	Free-free, outflow ?
26	18:14:13.46	-17:55:42.02	10.2 × 7.7	56	25.20 ± 13.88	60.35 ± 12.55	—	—	—	≤ 31.000	≤ 23.880	**	Free-free, outflow ?
27	18:14:14.10	-17:55:39.64	9.1 × 6.5	83	52.79 ± 18.23	113.00 ± 17.71	—	—	—	≤ 27.000	≤ 27.040	**	Free-free, outflow ?
28	18:14:13.78	-17:55:41.33	7.9 × 4.9	57	41.09 ± 17.04	53.23 ± 13.31	—	—	—	≤ 0.361	≤ 0.435	**	CO-contaminated
29	18:14:12.41	-17:55:08.30	10.1 × 7.9	96	7.63 ± 1.23	22.17 ± 1.79	16.7 × 14.3	—	77	0.70 ± 0.20	1.98 ± 0.20	**	Free-free, outflows
30	18:14:11.34	-17:55:19.55	10.1 × 9.0	89	16.18 ± 0.61	19.81 ± 0.71	—	—	—	≤ 0.409	≤ 0.410	**	Free-free, outflows
31	18:14:17.15	-17:55:29.83	6.4 × 4.2	70	10.34 ± 0.85	10.64 ± 0.69	11.1 × 9.1	—	38	0.81 ± 0.38	0.97 ± 0.38	**	Free-free, outflow ?
32	18:14:15.96	-17:55:22.22	9.3 × 6.6	59	10.71 ± 1.31	22.53 ± 1.28	13.1 × 11.4	—	111	2.09 ± 0.50	4.41 ± 0.50	**	Free-free, outflow ?
33	18:14:13.48	-17:56:05.49	9.4 × 8.6	10	7.90 ± 1.26	22.44 ± 1.58	—	—	—	≤ 0.535	≤ 0.558	**	Free-free, outflow ?
34	18:14:16.55	-17:56:20.48	10.2 × 5.7	66	5.08 ± 0.40	11.26 ± 0.46	—	—	—	≤ 0.024	≤ 0.025	**	Free-free, outflows
35	18:14:14.92	-17:55:48.80	23.7 × 5.2	122	11.15 ± 3.32	112.20 ± 7.20	21.7 × 13.3	—	117	26.18 ± 14.58	97.64 ± 20.25	**	Free-free, outflows
36	18:14:13.67	-17:55:23.94	7.1 × 5.4	39	20.96 ± 4.92	28.47 ± 3.84	—	—	—	≤ 1.842	≤ 1.843	**	Free-free, outflow ?
37	18:14:15.88	-17:55:32.39	8.9 × 6.8	56	5.97 ± 0.73	12.58 ± 0.79	—	—	—	≤ 0.409	≤ 0.410	**	Free-free, outflow ?
38	18:14:12.28	-17:55:30.87	12.6 × 7.0	39	2.78 ± 0.55	3.33 ± 0.99	—	—	—	≤ 0.191	≤ 0.222	**	Free-free, outflow ?
39	18:14:13.83	-17:55:52.23	8.8 × 7.7	41	24.71 ± 6.58	53.00 ± 5.95	16.6 × 12.6	—	180	20.90 ± 8.34	54.15 ± 8.36	**	Free-free, outflow ?
40	18:14:13.66	-17:55:26.01	9.0 × 6.8	59	16.11 ± 3.40	30.67 ± 2.96	—	—	—	≤ 2.736	≤ 2.740	**	Free-free, outflow ?
41	18:14:11.00	-17:55:42.02	6.8 × 5.7	80	16.64 ± 4.31	22.65 ± 3.49	14.9 × 12.4	—	8	3.30 ± 0.50	8.08 ± 0.51	**	Free-free, outflow ?
42	18:14:14.83	-17:55:32.25	12.9 × 8.1	89	5.06 ± 1.43	13.65 ± 2.70	—	—	—	≤ 0.806	≤ 0.972	**	Free-free, outflows
43	18:14:11.16	-17:55:39.70	9.0 × 7.4	40	14.11 ± 4.09	31.21 ± 3.85	14.1 × 12.1	—	21	3.26 ± 0.56	7.47 ± 0.56	**	Free-free, outflows
44	18:14:14.24	-17:55:15.40	9.8 × 7.6	59	7.15 ± 4.55	15.41 ± 4.42	11.7 × 8.7	—	54	26.10 ± 6.50	36.32 ± 6.53	**	Free-free
45	18:14:14.76	-17:55:45.88	12.0 × 8.5	117	19.69 ± 4.80	66.27 ± 5.59	17.5 × 13.5	—	116	39.16 ± 17.92	112.10 ± 17.95	**	Free-free
46	18:14:13.96	-17:55:31.07	10.4 × 6.9	27	20.82 ± 4.60	53.37 ± 4.99	—	—	—	≤ 2.524	≤ 2.530	**	Free-free, outflow ?
47	18:14:13.77	-17:55:31.17	7.7 × 5.9	79	8.40 ± 3.35	12.45 ± 2.92	11.4 × 10.4	—	95	22.61 ± 5.02	34.81 ± 3.87	**	Free-free
48	18:14:14.39	-17:55:29.23	11.3 × 7.9	43	5.80 ± 1.74	15.06 ± 2.04	—	—	—	≤ 1.431	≤ 1.435	**	Free-free, outflow ?

49	18:14:12.30	-17:55:19.57	7.6 × 4.9	42	8.85 ± 1.63	11.39 ± 1.27	-	-	-	≤ 0.639	≤ 0.639	★	Outflows
50	18:14:15.55	-17:55:34.69	13.2 × 11.2	89	4.48 ± 0.65	19.80 ± 0.94	-	-	-	≤ 0.345	≤ 0.416	★	Outflows
51	18:14:10.96	-17:55:43.15	7.4 × 7.0	55	14.98 ± 4.18	24.61 ± 3.27	13.3 × 8.7	88	1.59 ± 0.49	1.59 ± 0.49	2.85 ± 0.49	★★	Outflows
52	18:14:14.29	-17:55:04.65	8.6 × 8.3	177	7.82 ± 1.72	19.01 ± 2.00	16.2 × 10.6	91	1.34 ± 0.58	1.34 ± 0.58	2.60 ± 0.58	★★	Free-free, outflow ?
53	18:14:13.43	-17:55:38.03	8.4 × 5.8	82	41.49 ± 17.70	64.64 ± 13.82	-	-	-	≤ 14.780	≤ 14.790	★★	Free-free, outflow ?
54	18:14:17.79	-17:55:06.23	6.4 × 5.0	57	11.65 ± 1.28	12.59 ± 1.39	8.7 × 8.4	178	2.37 ± 0.48	2.37 ± 0.48	2.70 ± 0.37	★★	Free-free, outflow ?
55	18:14:14.05	-17:55:56.11	9.1 × 8.8	143	10.87 ± 2.64	27.53 ± 2.57	10.8 × 8.1	130	15.66 ± 6.02	18.90 ± 4.64	18.90 ± 4.64	★★	Free-free, outflow ?
56	18:14:13.23	-17:56:08.42	9.3 × 7.7	146	4.79 ± 0.96	13.37 ± 1.20	12.9 × 9.0	140	0.75 ± 0.45	0.91 ± 0.47	0.91 ± 0.47	★★	Free-free, outflow ?
57	18:14:11.52	-17:55:38.33	12.0 × 10.0	10	9.97 ± 4.58	34.59 ± 4.97	15.5 × 13.0	51	1.70 ± 0.68	3.62 ± 0.68	3.62 ± 0.68	★★	Free-free, outflow ?
58	18:14:12.10	-17:55:22.24	7.7 × 5.5	72	9.02 ± 2.03	12.77 ± 1.58	-	-	-	≤ 0.015	≤ 0.016	★★	Free-free, outflow ?
59	18:14:13.90	-17:55:50.45	8.3 × 7.4	52	20.70 ± 6.09	37.94 ± 4.76	16.5 × 11.6	94	12.09 ± 6.47	15.50 ± 6.49	15.50 ± 6.49	★	Free-free, outflow ?
60	18:14:13.39	-17:55:05.08	24.3 × 15.0	1	3.07 ± 0.79	32.69 ± 2.13	21.1 × 15.4	175	1.21 ± 0.37	3.57 ± 0.65	3.57 ± 0.65	★	Free-free
61	18:14:14.52	-17:55:50.90	7.4 × 6.6	31	11.36 ± 4.51	18.04 ± 3.52	11.0 × 9.7	11	26.37 ± 11.95	36.60 ± 9.21	36.60 ± 9.21	★★	Free-free, outflow ?
62	18:14:11.00	-17:55:44.34	7.9 × 4.8	67	12.06 ± 3.35	15.53 ± 2.59	14.2 × 8.6	81	2.59 ± 0.57	4.65 ± 0.57	4.65 ± 0.57	★★	Free-free, outflow ?
63	18:14:13.43	-17:55:40.81	8.6 × 7.8	86	17.53 ± 11.06	33.73 ± 8.52	-	-	-	≤ 33.430	≤ 25.760	★★	Free-free, outflow ?
64	18:14:14.14	-17:55:28.31	7.7 × 5.1	80	16.71 ± 4.04	21.26 ± 3.13	16.3 × 9.5	52	8.04 ± 2.96	12.04 ± 2.98	12.04 ± 2.98	★★	Free-free, outflow ?
65	18:14:11.13	-17:56:31.60	8.9 × 7.0	36	4.96 ± 0.97	9.85 ± 0.88	11.8 × 8.1	52	0.96 ± 0.31	1.16 ± 0.31	1.16 ± 0.31	★★	Free-free, outflow ?
66	18:14:13.80	-17:55:54.88	9.4 × 8.4	157	13.12 ± 5.45	28.66 ± 4.25	13.3 × 10.2	160	26.95 ± 8.76	46.10 ± 6.76	46.10 ± 6.76	★★	Free-free, outflow ?
67	18:14:11.41	-17:55:35.83	7.7 × 5.0	54	14.90 ± 5.93	19.80 ± 4.58	17.7 × 9.5	43	2.26 ± 0.70	4.26 ± 0.70	4.26 ± 0.70	★★	Free-free, outflow ?
68	18:14:15.73	-17:55:07.27	14.4 × 12.7	145	2.04 ± 0.38	10.83 ± 0.65	25.9 × 17.1	98	0.48 ± 0.29	1.66 ± 0.41	1.66 ± 0.41	★★	Free-free
69	18:14:13.32	-17:55:48.55	9.3 × 6.1	93	6.78 ± 2.39	10.82 ± 2.80	-	-	-	≤ 1.662	≤ 1.664	★★	Free-free
70	18:14:10.21	-17:55:54.76	10.4 × 7.3	164	4.45 ± 1.38	10.25 ± 2.17	-	-	-	≤ 0.316	≤ 0.318	★★	Free-free
71	18:14:14.52	-17:55:24.86	10.8 × 6.6	87	3.73 ± 1.58	7.16 ± 1.99	12.3 × 8.6	92	14.07 ± 3.90	18.32 ± 3.01	18.32 ± 3.01	★★	Free-free
72	18:14:13.42	-17:55:15.72	11.3 × 7.6	96	9.10 ± 2.36	23.48 ± 2.98	15.2 × 13.0	130	1.27 ± 0.63	2.29 ± 0.63	2.29 ± 0.63	★★	Outflows
73	18:14:14.34	-17:55:07.15	9.6 × 8.6	104	5.90 ± 1.91	17.49 ± 2.40	-	-	-	≤ 0.461	≤ 0.481	★★	Outflows
74	18:14:14.73	-17:55:07.18	10.2 × 7.6	62	7.74 ± 2.78	20.92 ± 3.02	15.2 × 10.5	3	0.83 ± 0.58	0.98 ± 0.58	0.98 ± 0.58	★★	Outflows
75	18:14:9.23	-17:56:03.18	6.2 × 5.1	50	9.67 ± 2.26	12.46 ± 1.83	11.8 × 11.0	82	1.51 ± 0.46	2.61 ± 0.46	2.61 ± 0.46	★★	Outflows
76	18:14:13.50	-17:56:23.42	21.9 × 18.3	94	1.69 ± 0.51	16.03 ± 1.18	-	-	-	≤ 0.357	≤ 0.599	★★	Outflows
77	18:14:9.66	-17:56:00.17	8.7 × 7.1	31	9.03 ± 2.19	18.36 ± 1.91	18.7 × 10.5	26	0.67 ± 0.41	1.43 ± 0.41	1.43 ± 0.41	★★	Outflows
78	18:14:15.10	-17:56:00.97	9.3 × 7.8	77	3.70 ± 1.07	9.22 ± 1.16	12.6 × 8.9	84	5.69 ± 3.26	7.90 ± 2.51	7.90 ± 2.51	★★	Outflows
79	18:14:13.83	-17:55:22.56	9.0 × 5.8	89	14.77 ± 4.52	22.06 ± 3.66	20.1 × 16.1	130	8.30 ± 3.63	28.78 ± 3.64	28.78 ± 3.64	★★	Outflows
81	18:14:10.89	-17:56:26.27	7.1 × 6.0	157	2.81 ± 0.66	3.67 ± 0.83	-	-	-	≤ 0.149	≤ 0.149	★★	Outflows
82	18:14:12.99	-17:56:13.95	14.1 × 12.1	84	2.40 ± 0.78	12.41 ± 1.27	-	-	-	≤ 0.247	≤ 0.333	★★	Outflows
83	18:14:14.64	-17:56:01.05	10.6 × 7.0	93	7.51 ± 2.33	15.52 ± 2.11	13.6 × 9.2	80	13.85 ± 7.48	19.94 ± 5.77	19.94 ± 5.77	★★	Outflows
84	18:14:11.21	-17:55:37.38	6.4 × 4.8	60	7.00 ± 3.64	7.33 ± 2.84	17.1 × 13.6	97	1.38 ± 0.43	3.40 ± 0.44	3.40 ± 0.44	★★	Outflows
86	18:14:14.71	-17:55:47.75	9.3 × 6.7	102	8.18 ± 3.48	15.05 ± 2.72	13.8 × 11.5	4	13.19 ± 11.56	23.14 ± 8.91	23.14 ± 8.91	★★	Outflows
87	18:14:15.88	-17:55:27.51	7.9 × 6.4	51	4.21 ± 1.34	6.14 ± 1.17	15.6 × 14.1	99	0.48 ± 0.41	1.39 ± 0.41	1.39 ± 0.41	★★	Outflows
88	18:14:16.65	-17:55:35.53	20.1 × 14.9	7	3.53 ± 0.72	29.80 ± 1.81	24.3 × 22.5	1	0.36 ± 0.07	1.43 ± 0.11	1.43 ± 0.11	★	Outflows
89	18:14:13.06	-17:55:09.91	10.0 × 7.3	71	2.62 ± 1.23	6.22 ± 1.87	15.9 × 11.2	103	1.06 ± 0.21	1.93 ± 0.21	1.93 ± 0.21	★★	Outflows
90	18:14:10.92	-17:56:28.57	9.5 × 7.3	112	2.68 ± 0.70	7.33 ± 0.88	15.0 × 10.5	121	0.40 ± 0.23	0.59 ± 0.23	0.59 ± 0.23	★★	Outflows
92	18:14:15.47	-17:55:39.00	11.5 × 9.2	50	4.18 ± 0.81	17.21 ± 1.42	19.2 × 16.5	142	0.96 ± 0.05	3.40 ± 0.05	3.40 ± 0.05	★	Outflows
94	18:14:13.76	-17:55:15.57	9.4 × 5.9	76	9.69 ± 3.58	17.24 ± 3.18	-	-	-	≤ 0.924	≤ 0.925	★★	Outflows
95	18:14:10.51	-17:56:14.47	7.5 × 6.1	149	3.51 ± 1.17	5.31 ± 1.23	-	-	-	≤ 0.246	≤ 0.247	★★	Outflows
96	18:14:12.92	-17:55:13.36	15.9 × 11.3	66	4.71 ± 1.56	21.43 ± 2.19	-	-	-	≤ 0.676	≤ 0.676	★★	Outflows
97	18:14:12.84	-17:55:49.01	7.3 × 5.1	64	3.29 ± 0.90	3.30 ± 1.01	18.8 × 16.1	85	0.54 ± 0.41	1.75 ± 0.41	1.75 ± 0.41	★★	Outflows
100	18:14:12.71	-17:55:32.45	7.6 × 4.6	15	2.69 ± 1.04	2.30 ± 1.26	-	-	-	≤ 0.246	≤ 0.246	★★	Outflows
101	18:14:13.90	-17:55:12.17	10.5 × 8.1	4	7.33 ± 2.82	17.96 ± 2.86	-	-	-	≤ 0.766	≤ 0.769	★★	Outflows

Notes. ^(a) Cores extracted by both *gatsf* and *Gex2D* algorithms. A single star corresponds to a match only for location, a double star, corresponds to a match for the location, size and flux of the source. ^(b) Nature of the core. If nothing is written, the core is not contaminated by any emission and is considered of prestellar nature.